Search for Higgs boson pair production through vector boson fusion with the ATLAS detector at the LHC

Mihovilović, Marko

Master's thesis / Diplomski rad

2023

Degree Grantor / Ustanova koja je dodijelila akademski / stručni stupanj: **University of Split, Faculty of Science / Sveučilište u Splitu, Prirodoslovno-matematički fakultet**

Permanent link / Trajna poveznica: https://urn.nsk.hr/urn:nbn:hr:166:188249

Rights / Prava: Attribution 4.0 International/Imenovanje 4.0 međunarodna

Download date / Datum preuzimanja: **2025-01-23**

Repository / Repozitorij:

Repository of Faculty of Science

zir.nsk.hr

UNIVERSITY OF SPLIT

dabar

DIGITALNI AKADEMSKI ARHIVI I REPOZITORIJI

University of Split
Faculty of Science

Search for Higgs boson pair production through vector boson fusion with the ATLAS detector at the LHC

Master thesis

Marko Mihovilović

Split, September 2023.

First and foremost, I would like to express my heartfelt gratitude to my supervisor, doc. dr. sc. Toni Šćulac, for his amazing and highly educational classes and seminars. His motivation and guidance have been instrumental in inspiring me to pursue research in particle physics. I also want to thank him for his support and encouragement throughout my master's studies and for connecting me with my mentor.

I am extremely thankful to my mentor, dr. Luca Cadamuro, for welcoming me as his intern and providing me with the opportunity to conduct my research abroad. His wealth of knowledge, encouragement, support, and exceptional patience have been invaluable throughout this journey. I eagerly anticipate continuing my research as a Ph.D. student under his mentorship once again.

I would also like to extend my appreciation to the entire ATLAS group at the IJCLab in Orsay. Despite my limited proficiency in French, they welcomed me into the group and encouraged me to pursue a career as a researcher.

Lastly, a big thank you to my family and friends for always being there for me and always showing me support and belief in me.

Temeljna dokumentacijska kartica

Sveučilište u Splitu
Prirodoslovno – matematički fakultet
Odjel za fiziku
Ruđera Boškovića 33, 21000 Split, Hrvatska

Diplomski rad

Potraga za proizvodnjom parova Higgsovih bozona kroz fuziju vektorskih bozona s ATLAS detektorom u velikom hadronskom sudaraču

Marko Mihovilović

Sveučilišni diplomski studij Fizika, smjer Astrofizika i fizika elementarnih čestica

Sažetak:
U ovom radu prezentiraju se rezultati istraživanja VBF (fuzije vektorskih bozona) produkcije parova Higgsovih bozona i služi kao ključna osnova za nadolazeće ATLAS analize u kojoj će se koristiti podatci iz prošlih i budućih eksperimenata Velikog hadronskog sudarača (LHC). U početnom dijelu analize, istražuje se utjecaj anomalnih vrijednosti interakcija na produkciju parova Higgsovih bozona putem fuzije vektorskih bozona, otkrivajući značajno poboljšanje VBF produkcije pri višim vrijednostima m_{HH}. Istraživanje se proširilo na ubrzanu (eng. boosted) topologiju, ukazujući na do 40% poboljšanje analize za specifične vrijednosti interakcija. U drugoj fazi rada, ispitivan je kanal raspada $HH \to b\bar{b}\tau^+\tau^-$, za kojeg smo prikazali karakteristike raspadnutih čestica. Također odabrani kanal raspada se provjerava u ubrzanom režimu. Ovo sveobuhvatno istraživanje obogatit će buduća istraživanja omogućujući usporedbu prikupljenih podataka sa simulacijama te potaknuti na buduće pretrage ubrzane topologije u kontekstu fuzije vektorskih bozona koje dosad nisu bile istraživane.

Ključne riječi: Higgs bozon, LHC, Higgs bozon parovi, Fuzija vektorskih bozona, ATLAS

Rad sadrži: 45 stranica, 37 slika, 2 tablice, 20 literaturnih navoda. Izvornik je na engleskom jeziku.

Mentor: doc. dr. sc. Toni Šćulac

Neposredni voditelj: dr. sc. Luca Cadamuro

Ocjenjivači: doc. dr. sc. Toni Šćulac,
doc. dr. sc. Marko Kovač,
doc. dr. sc. Damir Lelas

Rad prihvaćen: 13.09.2023.

Rad je pohranjen u Knjižnici Prirodoslovno – matematičkog fakulteta, Sveučilišta u Splitu.

Basic documentation card

University of Split
Faculty of Science
Department of Physics
Ruđera Boškovića 33, 21000 Split, Croatia

Master thesis

Search for Higgs boson pair production through vector boson fusion with the ATLAS detector at the LHC

Marko Mihovilović

University graduate study programme Physics, orientation Astrophysics and elementary particle physics

Abstract:

This thesis delves into the VBF production of Higgs boson pairs (HH), serving as a crucial foundation for forthcoming ATLAS analyses using data from past and future LHC runs. Initial analysis explored the impact of anomalous couplings on Higgs pair production via vector boson fusion, revealing significant enhancements in VBF HH production rates at higher m_{HH} values. The study extended to the boosted topology, demonstrating up to 40% analysis improvement for specific coupling values. In the subsequent phase, the $HH \to b\bar{b}\tau^+\tau^-$ decay channel was examined, illuminating particle decay traits. The selected decay channel is also examined in the "boosted" regime. This comprehensive investigation enriches future explorations, enabling data-simulation comparisons and reinforcing boosted regime searches that have not been explored yet.

Keywords: Higgs boson, LHC, Higgs boson pairs, Vector boson fusion, ATLAS

Thesis consists of: 45 pages, 37 figures, 2 tables, 20 references. Original language: English.

Supervisor: doc. dr. sc. Toni Šćulac

Leader: dr. sc. Luca Cadamuro

Reviewers: doc. dr. sc. Toni Šćulac,
doc. dr. sc. Marko Kovač,
doc. dr. sc. Damir Lelas

Thesis accepted: September 13, 2023

Thesis is deposited in the library of the Faculty of Science, University of Split.

Contents

1 Introduction

The groundbreaking discovery of the Higgs (H) boson by the ATLAS and CMS Collaborations in 2012 [1,2] marked a transformative chapter in the realm of experimental high-energy physics. Since its initial observation in 2012, rigorous efforts have been dedicated to comprehending the properties of the Higgs boson, including its interactions with other particles. Thus far, the observed characteristics of the Higgs boson have aligned with the predictions of the Standard Model (SM). The extremely rare process of generating a pair of Higgs bosons (HH) offers a distinctive avenue to explore the Higgs boson's trilinear coupling (self-coupling) and the quartic coupling involving two Higgs bosons and two vector bosons, both deeply connected to the theoretical foundations of the Brout-Englert-Higgs mechanism. The dominant mechanisms for HH production at the Large Hadron Collider are gluon-gluon fusion (ggF) and vector boson fusion (VBF). In this study, we delve into the nonresonant production of HH through vector boson fusion (VBF HH). The standard model calculates the cross-section for this second most prevalent HH production mechanism to be $\sigma_{\text{VBF}} = 1.726 \pm 0.036$ fb at $\sqrt{s} = 13$ TeV , as computed at the next-to-next-to-next-to leading order (N3LO) within the quantum chromodynamics (QCD) perturbative expansion [3]. Our focus revolves around three distinctive types of Higgs boson couplings: the Higgs boson self-coupling (HHH), the trilinear coupling between Higgs and vector bosons (VVH), and the quartic coupling linking two vector bosons and two Higgs bosons (VVHH). For these couplings, we introduce the parameter modifiers κ_λ, κ_V, and κ_{2V} (referred to as "coupling modifiers"), which quantify their strengths relative to the SM expectations.

While the HHH coupling can be explored via the ggF production mode and the VVH coupling is constrained by analyses of single Higgs boson production and decay rates, the VBF HH process furnishes a distinctive avenue to probe the quartic VVHH coupling. While in the SM, $\kappa_{2V} = \kappa_V = \kappa_\lambda = 1$, several models of physics beyond the SM (BSM) break this constraint. Consequently, the VBF cross-section can significantly increase for anomalous values of these coupling parameters, particularly in the high HH invariant mass phase space.

Amongst the VBF production mode, this study specifically targets the final state where one Higgs boson decays into a bottom (b) quark-antiquark pair, while the other undergoes a tau-antitau decay. This final state was chosen because it benefits of a sizeable branching ratio of $B(HH \to b\bar{b}\tau^+\tau^-) = 7.3\%$ [4] and of a reduced background contamination, making it one of the most sensitive to HH production

In experimental terms, the VBF process is defined by the presence of two widely separated jets with a substantial dijet invariant mass. These VBF jets are located in the forward part of the detector, whereas the HH decay products are located at the central region. While previous analyses mostly concentrated on resolved event topologies, which reconstruct each of the decay products as distinct jets, our analysis focuses on Higgs bosons with high Lorentz boost,

resulting in tightly collimated decay products. This often precludes the individual reconstruction of each decay particle. Consequently, each decay particle is reconstructed as a large-radius jet characterized by distinctive substructure. Since anomalous values of kappas lead to enhancement of VBF production at high m_{HH}, where we want to study high transverse momentum (p_T) Higgs bosons from collimated decay products, and this 'boosted' topology hasn't been explored for the promising $b\bar{b}\tau^+\tau^-$ channel, there is an urge for this study.

Therefore, the primary objective of this study is to simulate this process and quantify the proportions of total boosted events for various coupling scenarios, in order to evaluate the potential improvements that can be achieved by developing a new analysis that focuses on the boosted regime.

2 Theoretical overview

2.1 Standard model

The underpinning of our understanding of the physical universe lies in the realm of quantum field theory, with the SM as its foremost description of the fundamental constituents of matter and their interactions. This theoretical framework accounts for a limited set of elementary particles that compose the universe. Among these particles are electrons, protons, neutrons, and neutrinos, each engaging in intricate interactions through three primary forces: electromagnetic, strong nuclear, and weak nuclear. While electrons orbit atomic nuclei due to electromagnetic forces, the strong nuclear force binds protons and neutrons within nuclei. Furthermore, weak nuclear forces govern processes like β decay, involving electrons, protons, neutrons, and neutrinos [5].

Upon delving into energy scales higher than those observable in everyday life, the intricacy of the particle world becomes more apparent. Our preconceived notion that protons and neutrons were indivisible building blocks is challenged. Instead, they are composed of smaller, elemental constituents known as quarks. These quarks, governed by Quantum Chromodynamics (QCD), interact through the strong nuclear force exchanging gluons, who act as the carriers of this interaction. Quarks possess a "color charge," analogous to electric charge, which confines them into composites called hadrons. The phenomenon of hadronization arises when color-charged objects fragment, producing collimated groups of particles collectively referred to as jets [5]. These jets hold paramount importance in the analysis outlined in this thesis.

Interactions stemming from electric charges are mediated by the exchange of photons, a phenomenon central to the electromagnetic force. In contrast, the weak nuclear interaction involves W^+ and W^- bosons (charged-current) as well as Z bosons (neutral current). These gauge bosons, characterized by their spin-1, enable the mediation of weak interactions [5].

The SM organizes elementary particles into three distinct generations, each distinguished by particle mass and properties. Fig. 1 offers a visual representation of this organization. The first generation comprises familiar entities like the electron neutrino, up quark, down quark, and electron. The second generation introduces particles such as the muon neutrino, strange quark, charm quark, and muon. Lastly, the third generation includes the tau neutrino, top quark, bottom quark, and tau lepton.

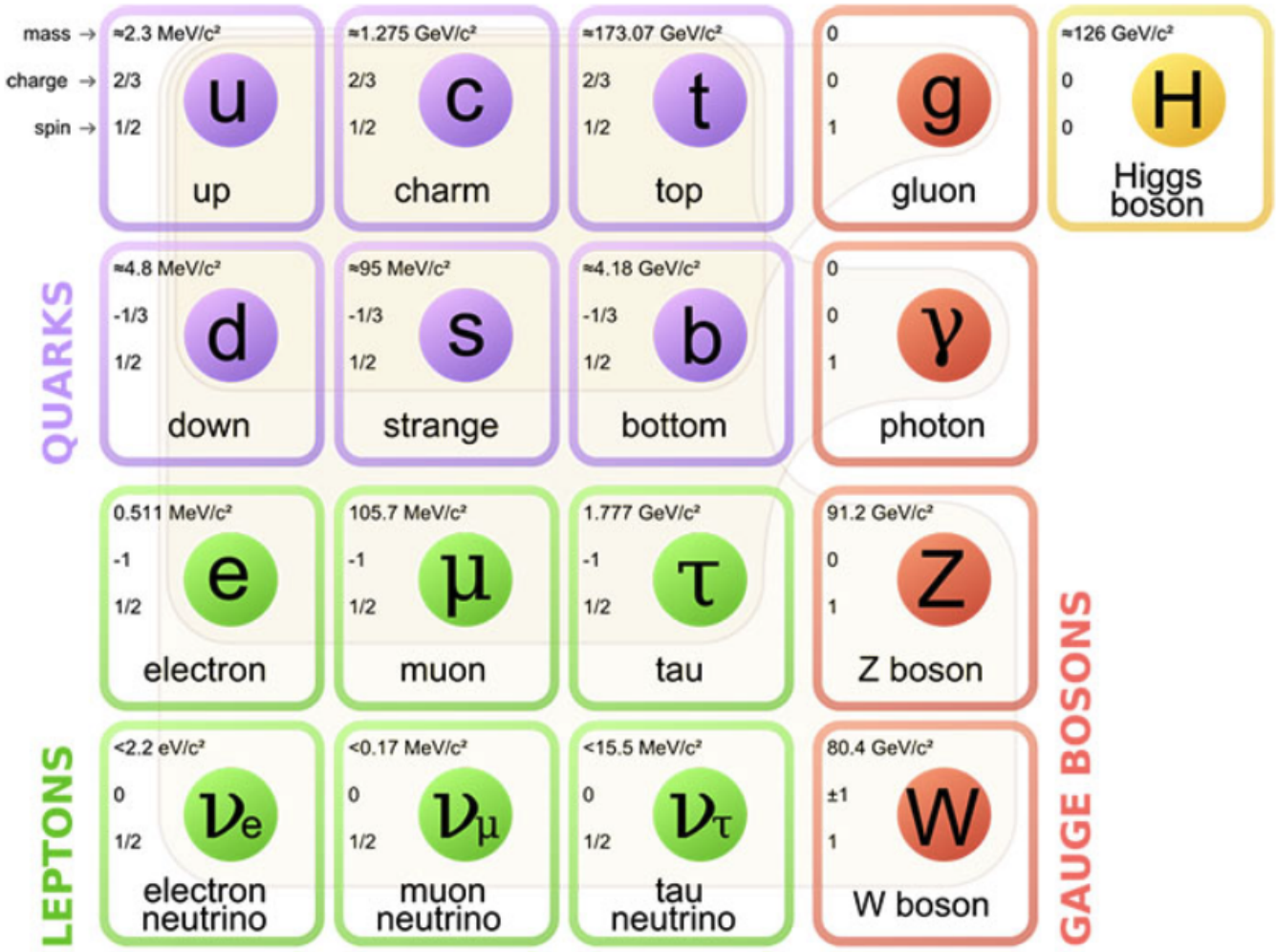

Figure 1: *Elementary particles of the Standard Model. Taken from[6]*

The final component of the Standard Model is the Higgs boson, discovered at the LHC by the ATLAS and CMS experiments in 2012 [1,2]. The Higgs boson, with a mass of approximately 125 GeV, is distinct from all other particles in the Standard Model. It is a spin-0 scalar particle, unlike the spin-half fermions and spin-1 gauge bosons. The Higgs boson plays a crucial role in the theory as it endows other particles with mass through their interaction with the Higgs field [5].

Although the Higgs boson represents a pivotal component of the SM, numerous questions and mysteries remain to be elucidated. While its existence has been confirmed, a comprehensive understanding of its properties and behaviors is still underway. By continuing to study the Higgs boson, we have the opportunity to gain deeper insights into the broader realm of particle physics.

In addition to the ongoing exploration of the Higgs boson's properties, it is imperative to extend our scientific inquiries beyond the boundaries of the Standard Model. Despite the significant achievements of the Standard Model in characterizing the fundamental particles

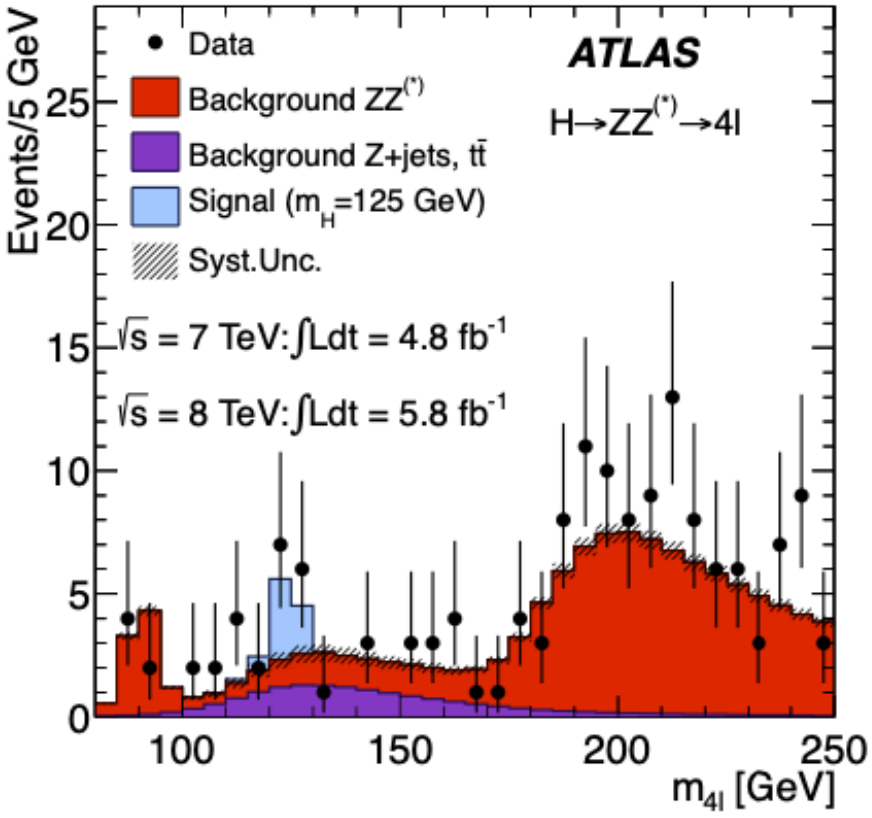

Figure 2: *The distribution of the four-lepton invariant mass, m_{4l}, for the selected candidates, compared to the background expectation in the 80–250 GeV mass range, for the combination of the $\sqrt{s}$ = 7 TeV and $\sqrt{s}$ = 8 TeV data. The signal expectation for a SM Higgs with m_H = 125 GeV is also shown. Taken from [7]*

and their interactions, it falls short in addressing various observed phenomena in the universe. Among these are the enigmas of gravity, dark matter, and neutrino mixing and mass.

Gravity stands as one of the four fundamental interactions, yet its description eludes the Standard Model's grasp. Its distinct nature, contrasting starkly with the other three forces, has rendered the task of unifying them exceedingly challenging. The framework of Einstein's General Relativity (GR) has successfully articulated gravity's principles, though bridging it with the Standard Model presents an intricate dilemma. A proposed approach involves introducing a novel mediator field associated with gravity — the hypothetical graviton particle — a concept still devoid of experimental validation [8].

Furthermore, empirical insights drawn from astronomical observations divulge that only a mere 5% of our universe's matter and energy composition can be attributed to ordinary matter, consisting of hadrons and leptons. The remaining 95% encompasses the realms of dark matter (25%) and dark energy (70%), territories untouched by the Standard Model's explanations or candidate solutions [8].

The realm of neutrinos, once considered massless entities within the Standard Model, has

been shaken by the revelations of flavor oscillation, hinting at their possession of nonzero mass. The implications of this phenomenon raise intriguing questions about whether these slight neutrino masses can emanate from the same electroweak symmetry-breaking mechanism that underpins the other elemental particles in the Standard Model.

The challenges faced by the SM have paved the way for the emergence of theories that extend beyond its boundaries, referred to as beyond-the-SM (BSM) theories. In a similar context, this study aims to investigate scenarios that deviate from the predictions of the standard model. Even if the energy scale of BSM physics cannot be directly reached by the LHC, evidence of this new physics can still be uncovered through measurements of other properties such as the self-coupling and the VVHH interaction.

2.2 The Brout-Englert-Higgs mechanism

The Brout-Englert-Higgs (BEH) mechanism, is a mechanism that provides a theoretical framework, based on the concept of spontaneous symmetry breaking, for understanding the mass of fundamental particles within the context of quantum field theory. This concept arises when the inherent symmetries of a physical system are not mirrored by the individual ground states of the system. In the BEH mechanism, the existence of a complex scalar doublet of fields is proposed, in order to realize spontaneous symmetry breaking, as:

$$\Phi = \begin{pmatrix} \phi_+ \\ \phi_0 \end{pmatrix} \tag{2.1}$$

The field has an hypercharge Y_Φ = 1 making its covariant derivative:

$$D_\mu = \partial_\mu - igW_\mu^i \frac{\sigma_i}{2} - \frac{1}{2} ig' B_\mu \tag{2.2}$$

Now BEH lagrangian can be written as:

$$\mathscr{L}_{\text{BEH}} = (D_\mu \Phi)^\dagger (D_\mu \Phi) - V(\Phi^\dagger \Phi) \tag{2.3}$$

These fields are governed by a potential function with a specific form

$$V(\Phi^\dagger \Phi) = -\mu^2 \Phi^\dagger \Phi + \lambda (\Phi^\dagger \Phi)^2 \tag{2.4}$$

with $\mu^2, \lambda > 0$. This potential is minimal for non-zero field values defined by the relation

$$|\Phi^2| = \frac{\mu^2}{2\lambda} \equiv \frac{v^2}{2} \tag{2.5}$$

The constant v is known as the vacuum expectation value. If the potential symmetry undergoes spontaneous breaking, transitioning to a ground state, the field can be written as:

$$\Phi(x) = \frac{1}{\sqrt{2}}\exp\left[\frac{i\sigma_i\theta^i(x)}{v}\right]\begin{pmatrix}0\\v+H(x)\end{pmatrix} \tag{2.6}$$

Eq. 2.6 contains the presence of a real scalar massive field, denoted as H, and three massless fields represented by θ_i. However, these unobserved massless bosons can be eliminated using an SU(2)$_L$ transformation with a specific gauge referred to as the "unitary gauge":

$$\Phi(x) \to \Phi'(x) = \exp\left[\frac{-i\sigma_i\theta^i(x)}{v}\right]\Phi(x) = \frac{1}{\sqrt{2}}\begin{pmatrix}0\\v+H(x)\end{pmatrix} \tag{2.7}$$

By substituting $\Phi(x)$ and Eq. 2.2 in Eq. 2.3, the BEH Lagrangian becomes:

$$\begin{aligned}\mathscr{L}_{BEH} = &\frac{1}{2}\partial_\mu H\partial^\mu H - \frac{1}{2}(2\lambda v^2)H^2\\ &+\left[\left(\frac{gv}{2}\right)^2 W^\mu W^-_\mu + \frac{1}{2}\frac{(g^2+g'^2)v^2}{4}Z^\mu Z_\mu\right]\left(1+\frac{H}{v}\right)^2\\ &+\lambda v H^3 + \frac{\lambda}{4}H^4 - \frac{\lambda}{4}v^4\end{aligned} \tag{2.8}$$

The first line in Eq. 2.8 represents the evolution of the scalar Higgs field, with its corresponding mass $m_H^2 = 2\lambda v^2$. When the potential symmetry undergoes spontaneous breaking, three of the four degrees of freedom associated with the field Φ manifest as the longitudinal polarizations of the $W^\pm$ and Z bosons. Consequently, the masses of these bosons arise from this mechanism, as observed in the second line of Eq. 2.8. Alongside their masses, the second line also describes the interactions of the weak bosons with the Higgs field. There are HWW and HZZ interactions from the $2H/v$ term, and HHWW and HHZZ interactions from the H^2/v^2 term. Lastly, the third line presents the prediction for cubic and quartic self-interactions of the Higgs boson.

The values of the trilinear (H^3) and quadrilinear (H^4) self-interactions are determined by the parameter λ, which governs the shape of the scalar potential described by Equation (2.4). Thus, the strength of these interactions directly depends on the specific form of the potential. An essential physics objective in the experimental investigation of HH production is to directly measure λ, enabling a probing of the underlying shape of the scalar potential. Within the framework of the SM, a specific relationship is predicted for the value of λ:

$$\lambda = \frac{m_H^2}{2v^2} \approx 0.13 \tag{2.9}$$

Where the precise measurement of m_H = 125.25±0.17 GeV and of $v \approx 246$ GeV leads to a

precise prediction of λ [7]. Consequently, the study of HH interactions becomes a means to test the consistency of the SM and verify the realization of the BEH mechanism in nature.

Examining this interaction goes beyond simply confirming an unmeasured property of the SM. The coupling of the Higgs boson with fermions is intricately linked to the Yukawa coupling structure, while its interactions with vector bosons are associated with the breaking of electroweak symmetry and the local quantization around the minimum of the scalar potential [4]. In contrast, the self-interaction of the Higgs boson is dependent on a global shape property of the potential, representing a fundamental aspect of the BEH mechanism. Therefore, measuring the Higgs boson self-coupling would serve as confirmation that the scalar potential described by Equation (2.4) indeed exists in the natural world, providing valuable insights into its properties. Given its profound connection with the fundamental principles of the SM, exploring the self-coupling of the Higgs boson has implications for our understanding of the evolution of the universe. This holds paramount importance as the stability of this vacuum resonates with the overall stability of the universe itself [9]. A comprehensive grasp of the self-coupling of the Higgs boson plays a pivotal role in our ability to foresee whether the universe remains stable in its current state or if it might venture into a transformative phase.

2.3 HH Production Modes

Since the discovery of the Higgs boson in 2012, a primary objective of the ATLAS and CMS collaborations has been to deepen our comprehension of its properties and interactions. Understanding the Higgs self-coupling holds paramount significance in unraveling the mechanism behind electroweak symmetry breaking, and it serves as a test of the electroweak theory. Notably, the production of Higgs boson pairs offers a direct means to explore the Higgs self-coupling, as it profoundly impacts the size of the HH production cross-section [3]. This entails considering the conventional production channels in which the Higgs boson is produced singly, but with the possibility for the Higgs state to be off mass-shell and subsequently decay into two real Higgs bosons. Researchers have proposed four primary categories of processes for the production of Higgs boson pairs, listed bellow in decreasing order of their cross section [10]:

- the gluon fusion mechanism, $gg \rightarrow HH$ which is mediated by loops of heavy quarks (mainly top quarks) that couple strongly to the Higgs boson
- the WW/ZZ fusion processes (VBF), $qq' \rightarrow V^*V^*qq' \rightarrow HHqq'$ ($V = W, Z$), which lead to two Higgs particles and two jets in the final state
- the double Higgs–strahlung process, $q\bar{q}' \rightarrow V^* \rightarrow VHH$ ($V = W, Z$), in which the Higgs bosons are radiated from either a Wor a Z boson

- associated production of two Higgs bosons with a top quark pair, $pp \rightarrow t\bar{t}HH$

The experimental investigation so far has been focused on the two main production modes, the fusion of gluons (ggF) and of vector bosons (VBF).

2.3.1 ggF Production

In the framework of the SM, the gluon-gluon fusion process (ggF) accounts for more than 90% of non-resonant Higgs boson pair (HH) production. At leading order (LO), this process involves two diagrams, namely the triangle diagram and the box diagram, depicted in Figure 3. The triangle diagram involves the Higgs boson trilinear self-coupling, λ_{HHH}. These diagrams exhibit destructive interference, resulting in a relatively small cross-section for SM HH production, which is three orders of magnitude lower compared to single Higgs boson production. It is sufficient to note that within the Standard Model, the values of the self-couplings are such that $\lambda_{HHH} = \lambda_{HHHH} = \lambda$.

The SM prediction for the ggF-produced HH cross-section is $\sigma^{SM}_{ggF}(HH) = 31.05^{+6\%}_{-23\%}(scale + mtop)\pm 3.0\%(PDF + \alpha_s)$ fb [3], calculated at next-to-next-to-leading order (NNLO) in α_s and incorporating an approximation of finite top-quark-mass effects . This prediction is based on a Higgs boson mass of m_H = 125 GeV and $\sqrt{s}$ = 13 TeV [3].

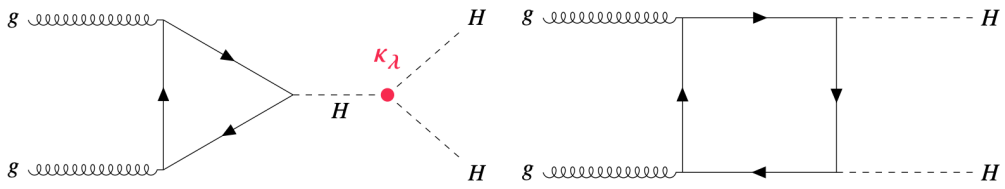

Figure 3: *Leading order Feynman diagrams showing ggF non-resonant production of pairs of Higgs bosons in the Standard Model: (a) the triangle diagram, featuring the Higgs boson trilinear self-coupling, labeled with the self-coupling modifier $\kappa_\lambda \equiv \lambda$ / λ_{SM} and (b) the box diagram, featuring only a loop of quarks. Taken from[3]*

To investigate the potential effects of physics beyond the Standard Model on Higgs boson pair production, a straightforward method involves examining scenarios where the self-coupling values deviate from the predictions of the SM. By varying κ_λ, we can explore the impact of different coupling strengths on the HH production process. Out of all the production modes of Higgs boson pairs, the ggF process has received significant attention, primarily due to its high production rate.

2.3.2 VBF Production with Anomalous Couplings

Among the various HH production modes, the vector boson fusion process stands out as an intriguing option due to its unique characteristics. It represents the second-largest contribution to HH production and offers access to the coupling between one or two Higgs bosons and two vector bosons. Despite its relatively small production cross section, $\sigma^{SM}_{ggF}(HH) = 1.726^{+0.03\%}_{-0.04\%}(scale)\pm 2.1\%(PDF + \alpha_s)$ fb [3], determined at next-to-next-to-next-to-leading order (N3LO) precision for $\sqrt{s}$ = 13 TeV, the distinctive VBF topology presents a valuable means to identify signal events [10]. This is attributed to its two forward jets, which are well separated in pseudorapidity (η) and exhibit a large invariant mass. The leading-order Feynman diagrams for VBF HH production are illustrated in Fig. 4.

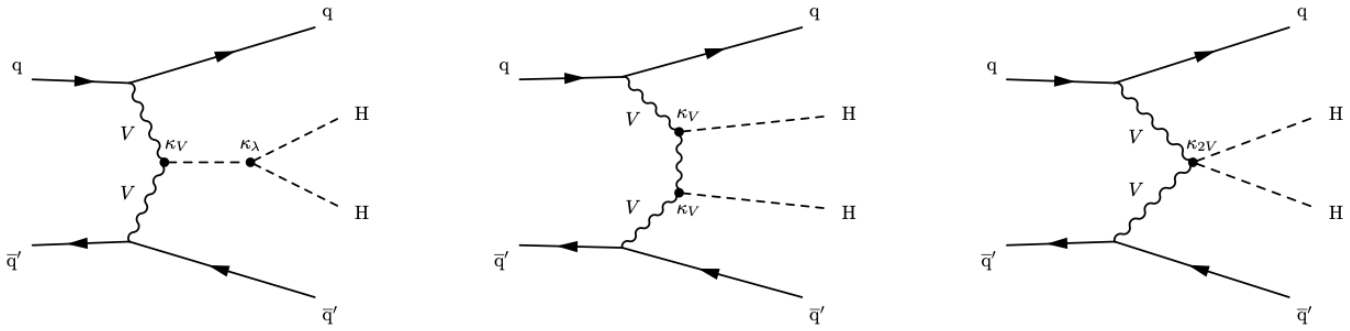

Figure 4: *Feynman diagrams contributing to Higgs boson pair production via vector boson fusion in the SM at leading order. The different H interactions are labelled with the coupling modifiers κ. Taken from[12]*

As depicted in Figure 4's Feynman diagrams, vector boson fusion (VBF) HH production involves the VVH and VVHH couplings (where $V = W, Z$). The strengths of these interactions relative to their Standard Model (SM) predictions are denoted by the coupling modifiers κ_V and κ_{2V}, respectively. In the SM, both interactions arise from the spontaneous breaking of electroweak symmetry, making their values connected through the same fundamental mechanism. Consequently, an amplitude cancellation occurs for longitudinally polarized vector bosons [4]. For generic κ_V and κ_{2V} couplings, at energies lower than the scale of new physics, the amplitude is dependent on the coupling strengths and the energy $\sqrt{\hat{s}}$ like

$$\mathscr{A}(V_L V_L \to HH) \approx \frac{\hat{s}}{v^2}(\kappa_{2V} - \kappa_V^2) \tag{2.10}$$

[19]. In the context of the Standard Model (SM), where $\kappa_V = \kappa_{2V} = 1$, this amplitude is suppressed. However, in scenarios where the Higgs boson originates from new strong dynamics at the TeV scale, deviations from the usual values of κ_V or κ_{2V} can lead to significant enhancements in the vector boson fusion HH production rate at high m_{HH}. In later sections of this paper, we will present the results of our simulations and demonstrate how anomalous values of κ_V and κ_{2V} can impact the VBF production.

2.4 HH Decay Channels

Due to the numerous possible decays of the Higgs boson, HH production leads to a wide array of phenomenologically rich final states, as illustrated in Figure 5. When selecting a specific final state for experimental searches, one Higgs boson is typically required to decay either to bb or WW to ensure a substantial branching fraction. The choice of the decay mode for the second Higgs boson involves a trade-off between the abundance of the final state and the level of background contamination.

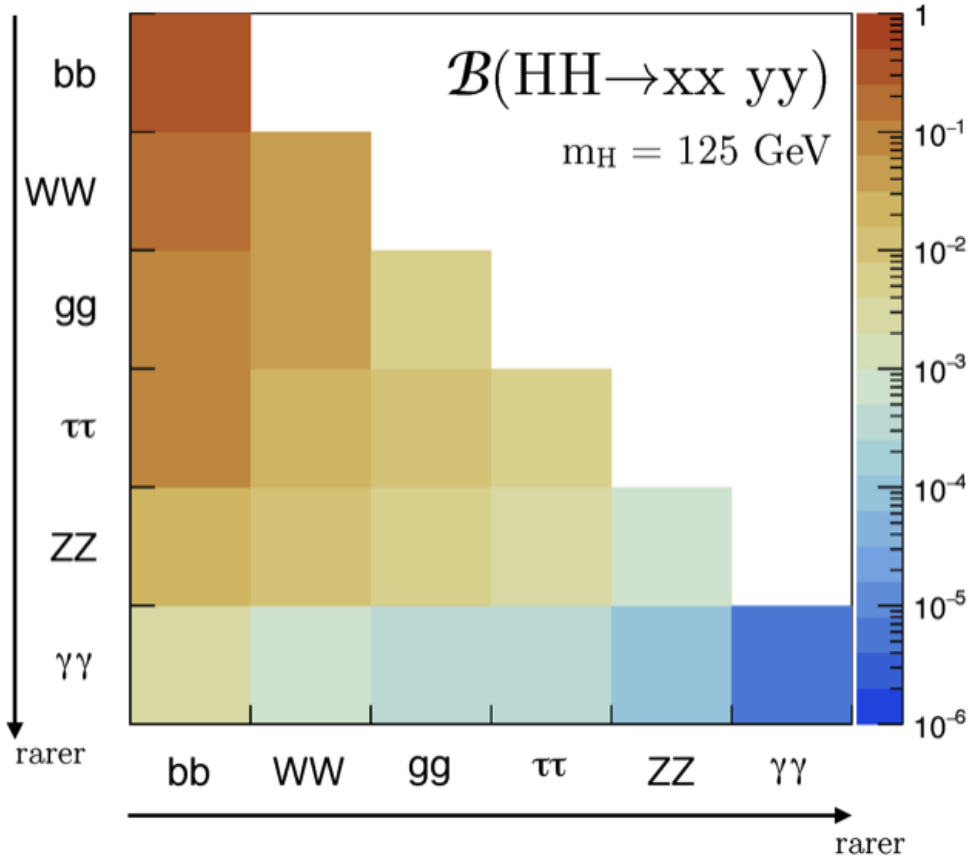

Figure 5: *Branching fractions for the main HH final states. Taken from[4]*

In my analysis, I will specifically direct my attention to the $b\bar{b}\tau^+\tau^-$ decay channel among the various possibilities. This particular decay channel, while not as investigated for the boosted regime as certain others, provides a valuable and diverse information. Through observation and analysis of the particle properties arising from this decay, we can attain significant insights their interactions with the Higgs boson. This channel holds specific interest due to its noteworthy branching ratio, being second in significance when considering that WW decay is typically explored with at least one leptonic W. Additionally, due to its limited background contributions, this channel emerges as one of the most sensitive avenues for exploration.

The $HH \rightarrow b\bar{b}\tau^+\tau^-$ decay mode exhibits one of the largest branching fractions (7.3%) among the investigated HH decay channels. The search for $b\bar{b}\tau^+\tau^-$ [3] involves distinct

signal regions targeting fully-hadronic, fully-leptonic and semi-leptonic di-τ final states, labeled $\tau_{\text{had}}\tau_{\text{had}}$, $\tau_{\text{lep}}\tau_{\text{lep}}$ and $\tau_{\text{lep}}\tau_{\text{had}}$ respectively, each characterized by its respective branching fractions as indicated in Table 1. The main irreducible backgrounds are $t\bar{t}$ and Z plus b jets production, plus instrumental backgrounds where hadronic jets are misidentified as τ and b jets [4].

Decay mode	Resonance	$\mathcal{B}$ (%)
Leptonic decays		35.2
$\tau^- \to \mathrm{e}^-\bar{\nu}_\mathrm{e}\nu_\tau$		17.8
$\tau^- \to \mu^-\bar{\nu}_\mu\nu_\tau$		17.4
Hadronic decays		64.8
$\tau^- \to \mathrm{h}^-\nu_\tau$		11.5
$\tau^- \to \mathrm{h}^-\pi^0\nu_\tau$	$\rho(770)$	25.9
$\tau^- \to \mathrm{h}^-\pi^0\pi^0\nu_\tau$	$\mathrm{a}_1(1260)$	9.5
$\tau^- \to \mathrm{h}^-\mathrm{h}^+\mathrm{h}^-\nu_\tau$	$\mathrm{a}_1(1260)$	9.8
$\tau^- \to \mathrm{h}^-\mathrm{h}^+\mathrm{h}^-\pi^0\nu_\tau$		4.8
Other		3.3

Table 1: *Weak decays of τ leptons and their branching fractions (*B*) in %. Taken from [20].*

As shown in Table 1, the final states resulting from hadronic tau decays contain charged hadrons and neutral pions. When identifying a "visible" hadronic tau candidate, which includes the decay products excluding neutrinos, it's essential that their reconstructed mass aligns with either the $\rho(770)$ or the $a1(1260)$ resonances. This alignment is observed in the $h^\pm\pi^0$ and $h^\pm\pi^0\pi^0$ or $h^\pm h^\mp h^\pm$ decay modes, respectively [20].

As we want to study processes in the high-mass regime, often exceeding 1 TeV, Higgs bosons can be produced with large momenta, causing their decay products to be collimated. In this context, standard reconstruction techniques are inefficient, as indicated by Figure 6, where reconstruction efficiency plateaus for $p_{T_{\text{vis}}} > 300\,\text{GeV}$.

Consequently, new techniques are being developed, known as the di-τ tagger. This technique enables the reconstruction and identification of boosted hadronically decaying $\tau^+\tau^-$ pairs. To facilitate identification, employment of a multivariate algorithm that distinguishes between $\tau^+\tau^-$ pairs and the multi-jet background stemming from quark- or gluon-initiated jets, leveraging information from calorimetric shower shapes and tracking data. Both the ATLAS and CMS experiments have recently updated their results of the searches for $b\bar{b}\tau^-\tau^+$ events using the full Run 2 data set [4]. In these analyses, events are categorized based on the tau decay modes ($\tau_{had}\tau_{had}$, $\tau_\mu\tau_{had}$, and $\tau_e\tau_{had}$), and the triggers used to select events in the case of ATLAS, or by the number of b-tagged jets and the topology (resolved, boosted, or VBF) in the case of CMS [4].

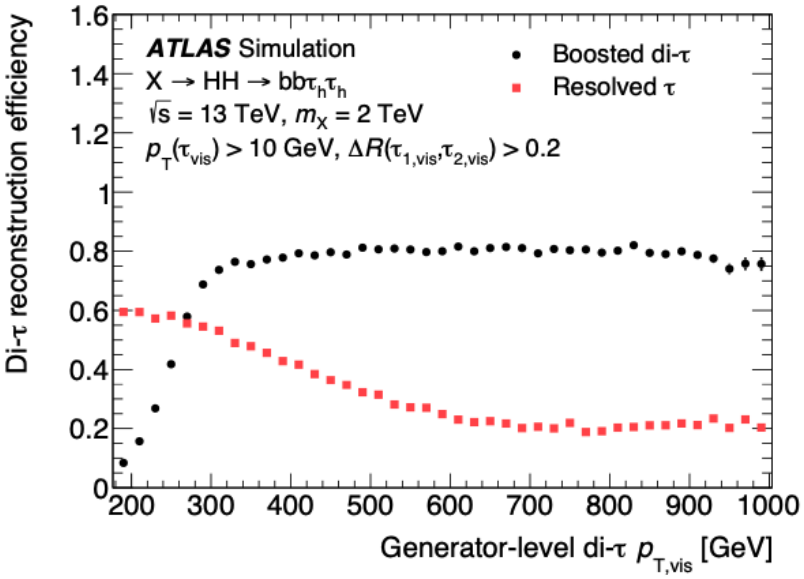

Figure 6: *Efficiency to reconstruct a di-τ system with (squares) resolved $\tau_{had\text{-}vis}$ objects and (circles) a boosted di-τ object versus the $p_{T_{vis}}$ of the di-τ system. Taken from[21]*

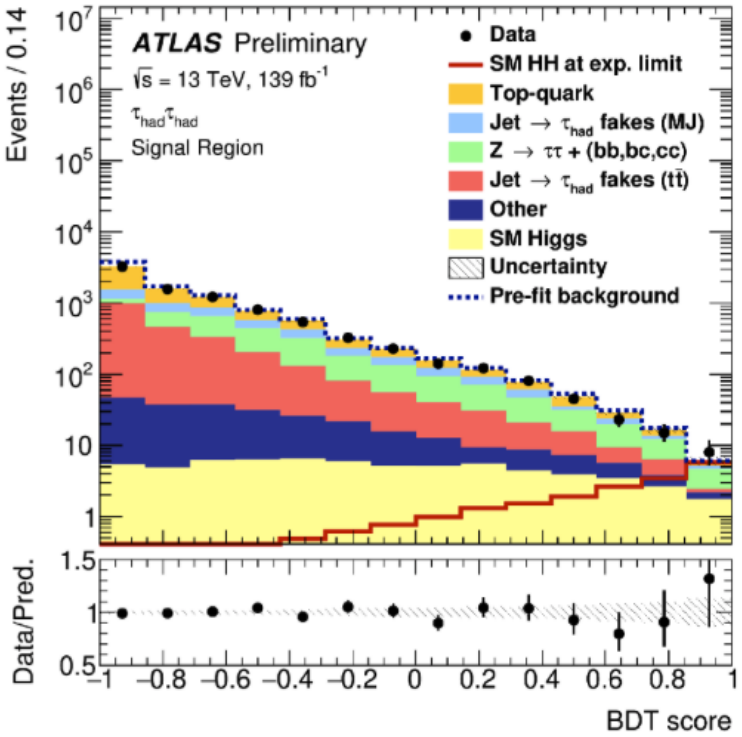

Figure 7: *The final fit distributions in the $b\bar{b}\tau^{-}\tau^{+}$ searches so far for the ATLAS BDT method. Output score for the most sensitive $\tau_{had}\tau_{had}$ (hadronic tau decays) category is shown. Taken from[4]*

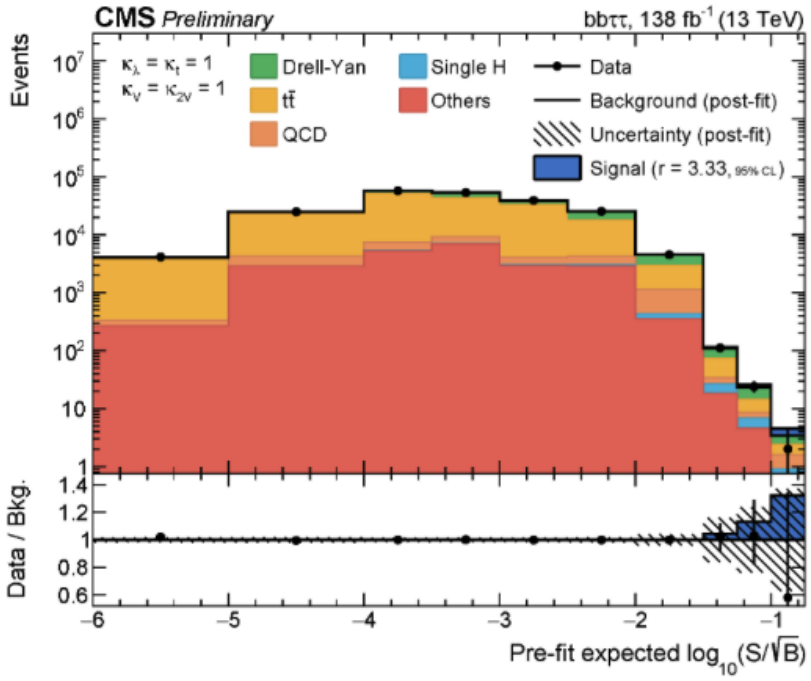

Figure 8: *The final fit distributions in the $b\bar{b}\tau^{-}\tau^{+}$ searches so far for the CMS aggregated DNN output score distribution. Results sorted by the log of the signal-to-background ratio are shown. Taken from[4]*

2.5 Current limits on coupling parameters

As mentioned earlier in the study, we will demonstrate how anomalous values of κ_λ, κ_V, and κ_{2V} can influence the VBF production rate. Numerous studies have endeavored to establish constraints on the ranges for these parameters.

Analyzing the observed (expected) 95% confidence level interval for κ_λ, studies show it to be $[-1.0, 6.6]$ ($[-1.2, 7.2]$), assuming all other Higgs boson couplings remain at their SM values [3]. These values for κ_λ are obtained from ggF analyses, as VBF is not as sensitive to κ_λ analyses compared to ggF.

On the other hand, the current VBF analyses reveal an observed (expected) 95% confidence level interval for κ_{2V} within the range $[0.62, 1.41]$ ($[0.66, 1.37]$), as depicted in Figure 9 [11]. The most stringent κ_{2V} results stem from the boosted bbbb analysis, as this process enhances in the high m_{HH} regime. Since there is currently no boosted $b\bar{b}\tau^{-}\tau^{+}$ analysis at the LHC, our focus will be on this analysis and the potential improvements in event acceptance that it can offer, aiming to enhance our existing constraints on the value of κ_{2V}.

For κ_V, the ranges allowed by these observed limits are $-1.2 < \kappa_V < -0.8$ or $0.8 < \kappa_V < 1.2$ [12]. In both instances, the observed limits closely mirror the expected median limits (depicted as dashed lines), implying that the anticipated ranges of exclusion closely align with the observed ones, as we can see in Figure 10 as well.

Figure 11 showcases the observed negative log-likelihood values as functions of the κ_{2V} and

κ_V couplings, with all other couplings held constant at their SM values. From the parabola shown in this figure, we can observe a cancellation that aligns with the cancellation we previously mentioned in Eq. 2.10. Concurrently, Figure 12 presents the outcome of the profile likelihood test statistic scan across the κ_λ-κ_{2V} plane.

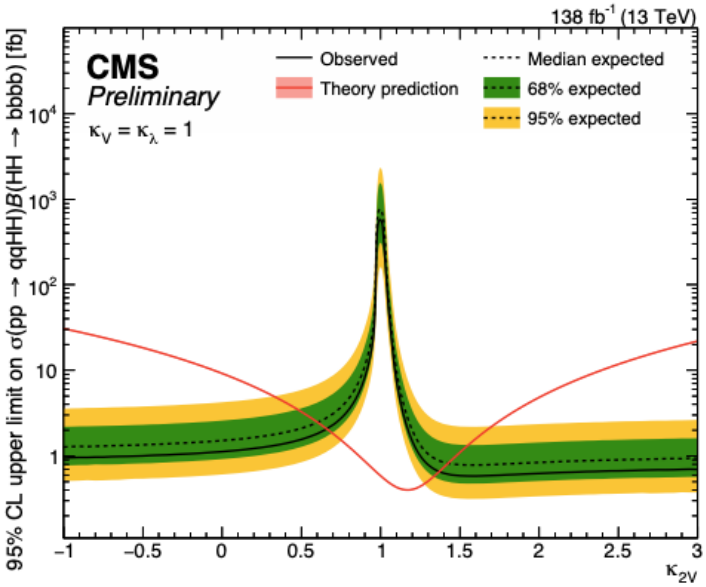

Figure 9: *Observed (solid line) and expected (dashed line) 95% CL exclusion limit on the product of the VBF HH production cross section and the branching fraction into bbbb, as a function of the κ_{2V} coupling, with other couplings fixed to the SM values. The crossings of observed limit and the theoretical cross section (red line) indicate the ranges of the coupling values excluded at 95% CL. Taken from[12]*

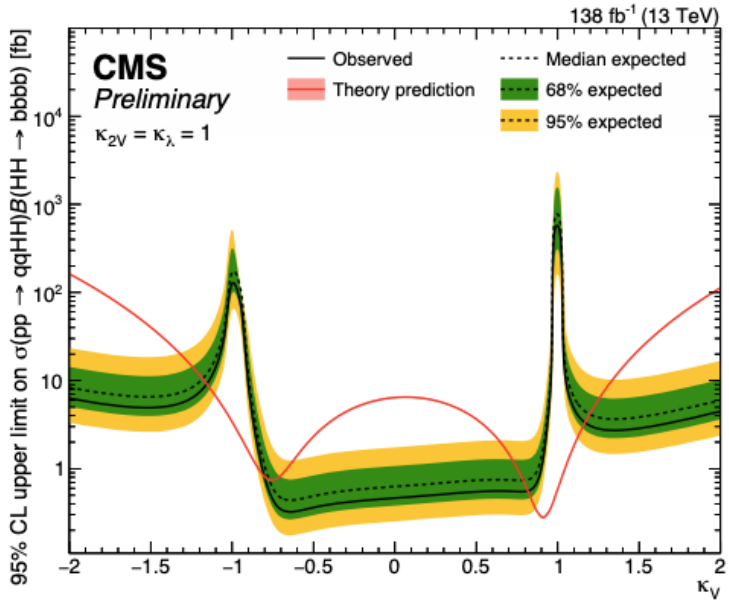

Figure 10: *Observed (solid line) and expected (dashed line) 95% CL exclusion limit on the product of the VBF HH production cross section and the branching fraction into bbbb, as a function of the κ_V coupling, with other couplings fixed to the SM values. The crossings of observed limit and the theoretical cross section (red line) indicate the ranges of the coupling values excluded at 95% CL. Taken from[12]*

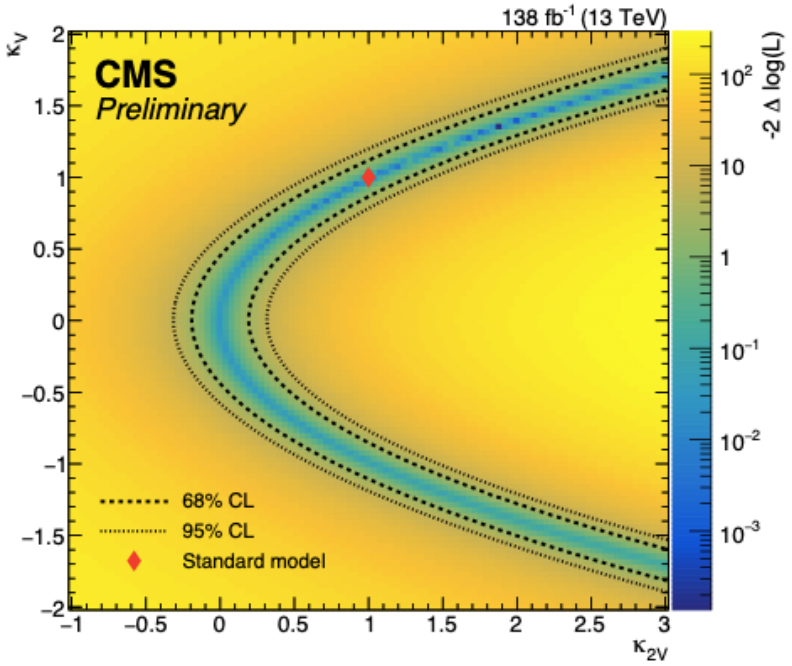

Figure 11: *Observed values of likelihood as a function of the κ_{2V} and κ_V couplings, assuming all the other couplings to be fixed to the SM values. Taken from[12]*

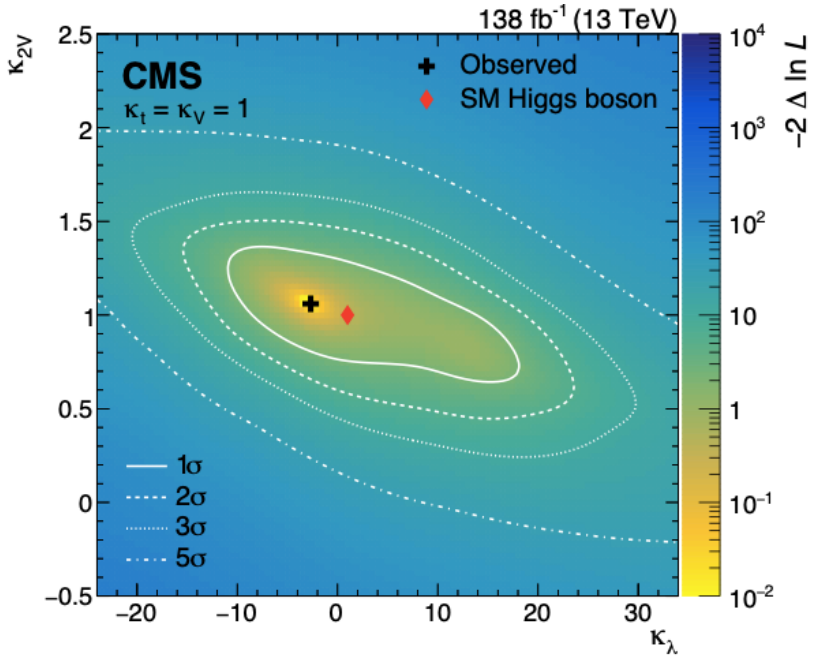

Figure 12: *Two-parameter profile likelihood test statistic $(-2\Delta\log(L))$ scan in data as a function of κ_λ and κ_{2V}. The black cross indicates the minimum, while the red diamond marks the SM expectation ($\kappa_\lambda = \kappa_{2V} = 1$). The gray solid, dashed, dotted, and dash-dotted contours enclose the 1, 2, 3, and 5 σ CL regions, respectively. Taken from [11].*

3 Experimental apparatus overview

3.1 ATLAS detector overview and physics requirements

The ATLAS detector and the trajectories of particles resulting from p-p collisions are described in terms of a specific coordinate system and nomenclature, which will be summarized briefly in this section. The origin of the coordinate system is designated as the nominal interaction point, with the z-axis aligned along the beam direction, and the $x - y$ plane perpendicular to the beam direction, as shown in Fig. 14. The positive x-axis points from the interaction point towards the center of the LHC ring, while the positive y-axis points upwards. The side-A of the detector is defined as the region with positive z, whereas side-C corresponds to the region with negative z.

The azimuthal angle ϕ is measured conventionally around the beam axis, and the polar angle θ represents the angle from the beam axis.

Pseudorapidity is defined as $\eta = -\ln(\tan(\theta/2))$. It is the massless limit of the rapidity, that is invariant for Lorentz boosts along the z-axis, hence why we use it. The distance ΔR in the pseudorapidity-azimuthal angle space is determined by $\Delta R = \sqrt{(\Delta\eta^2 + \Delta\phi^2)}$.

Transverse momentum p_T and missing transverse momentum p_{Tmiss} are defined as the projections of the corresponding vector quantities in the $x - y$ plane. Transverse momentum is a fundamental concept at hadron colliders that characterizes the motion of particles perpendicular to the beam direction. It is defined as the component of momentum in the transverse plane, which is orthogonal to the beam axis. We use it since it is the most "stable" indicator of a hard scatter interaction and a quantity that we know should conserve to 0.

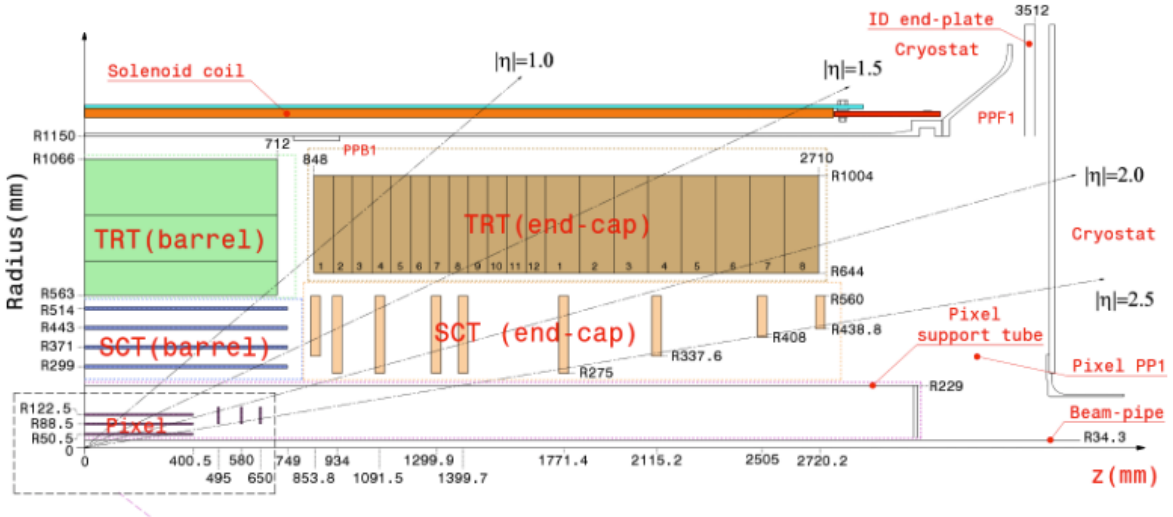

Figure 13: *The pseudorapidity (η) of a particle relative to the beam axis. Taken from [13]*

Other very important physical value is the cross section (σ). The cross section pertains to the likelihood of a specific particle interaction or event occurring. It quantifies the rate at which a particular reaction takes place during collision processes. Expressed in units of area, cross sections facilitate the comparison of different processes happening under the same experimental conditions.

Engineered to achieve comprehensive coverage, the ATLAS detector encompasses an array of components to fulfill this purpose. This system comprises an inner tracking detector, a superconducting solenoid, electromagnetic and hadronic calorimeters, and a muon spectrometer enhanced by three expansive superconducting toroidal magnets [14]. This framework maintains a symmetrical orientation in relation to the interaction point, exhibiting forward-backward symmetry. A slim superconducting solenoid encases the inner-detector cavity, while a triad of superconducting toroids, strategically positioned with eight-fold azimuthal symmetry around the calorimeters, supplements this configuration. Such design considerations have notably shaped the overall architecture of the detector.

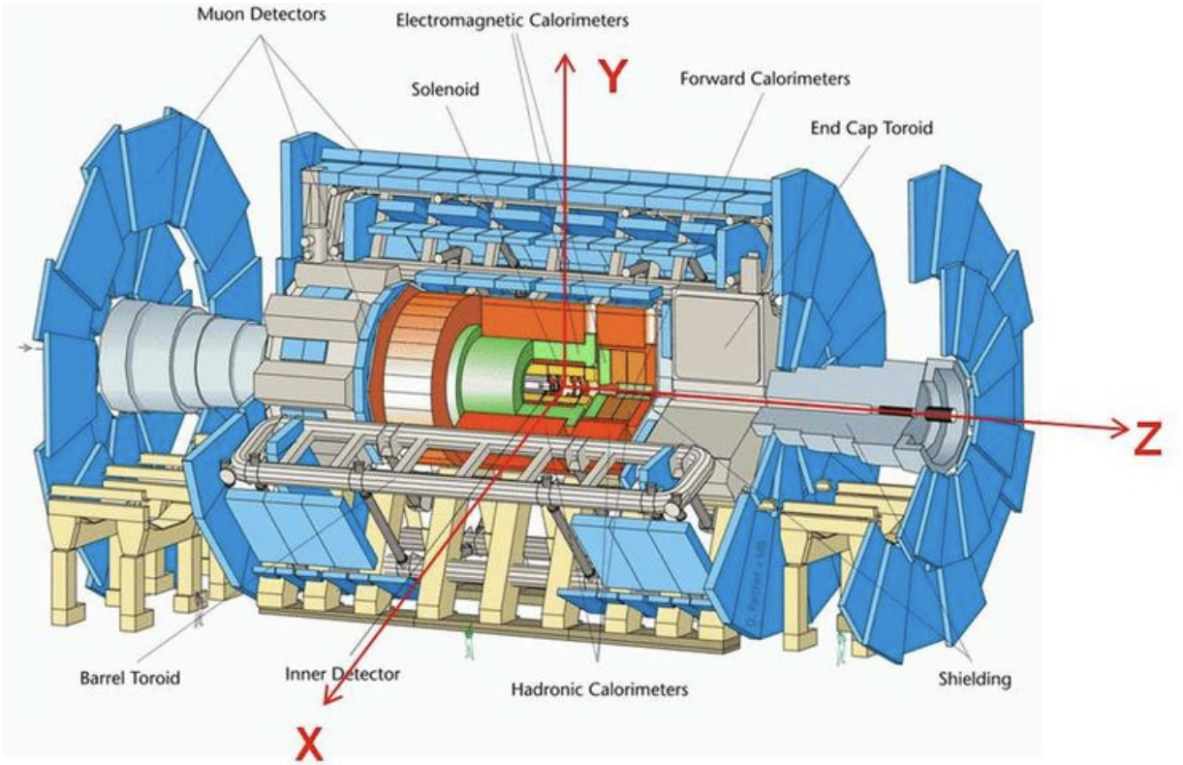

Figure 14: *Cut-away view of the ATLAS detector. Taken from [15]*

The inner detector operates within a 2T solenoidal field, utilizing both high-resolution semiconductor pixel and strip detectors and transition radiation tracker for pattern recognition, momentum, and vertex measurements, as well as electron identification.

For electromagnetic calorimetry, in the central region, within the range $|\eta| < 3.2$, high granularity liquid-argon (LAr) calorimeters with excellent energy and position resolution are employed. Hadronic calorimetry in the range $|\eta| < 1.7$ is performed by a scintillator-tile

calorimeter, consisting of a large barrel and two smaller extended barrel cylinders. In the end-cap regions ($|\eta| > 1.5$), LAr technology is used for the hadronic calorimeters, extending the coverage to the outer limits of the end-cap electromagnetic calorimeters. The LAr forward calorimeters provide measurements of electromagnetic and hadronic energy for the pseudorapidity coverage up to $|\eta| = 4.9$ [16], as in the forward part the absorption changes, hence the extension is necessary.

Surrounding the calorimeter system is the muon spectrometer, featuring an air-core toroid system with a long barrel and two inserted end-cap magnets. This configuration generates strong bending power while minimizing multiple-scattering effects, leading to excellent muon momentum resolution. The muon instrumentation includes trigger chambers with high timing resolution (approximately 1.5-4 ns). The dimensions of the ATLAS detector are defined by the muon spectrometer.

Considering the proton-proton interaction rate of approximately 40 MHz at the design luminosity of 10^{34} cm^{-2} s^{-1}, data recording is limited to about 200 Hz due to technological and resource constraints. To meet this requirement, an overall rejection factor of 5×10^6 against minimum-bias processes is necessary while maintaining high efficiency for new physics. The Level-1 (L1) trigger system utilizes a subset of detector information to make rapid decisions, reducing the data rate to approximately 75 kHz. The subsequent two levels, the Level-2 (L2) trigger and the event filter, collectively known as the high-level trigger, further reduce the data-taking rate to approximately 1 kHz [16].

4 Monte Carlo event generation

Monte Carlo simulations are powerful computational techniques used to model complex systems or processes through random sampling. In the context of high-energy particle physics analysis, Monte Carlo simulations are extensively utilized to study and predict the outcomes of particle interactions and collisions that occur at particle accelerators like the Large Hadron Collider or other experiments. These simulations play a crucial role in both theoretical predictions and experimental data analysis.

They are widely used in high-energy particle physics due to the inherently probabilistic nature of particle interactions. The simulations involve generating a large number of random events that obey specific physical laws based on theoretical models. These simulated events can then be compared to actual experimental data, enabling researchers to make predictions and interpret experimental results.

One of the main advantages of Monte Carlo simulations is their ability to handle complex multi-particle interactions that are challenging to calculate analytically. These simulations take into account higher-order processes, parton showers, and hadronization effects, making them crucial for obtaining realistic event predictions.

For the generation of the data sample required for our analysis, we utilized the ATLAS software framework, Athena. Developed in C++ with Python scripts for job configuration, Athena offers a robust platform to simulate particle collision events. This framework provides interfaces to a variety of general-purpose event generators, including Pythia6, Pythia8, MadGraph, Herwig, Herwig++, and Sherpa, as well as specialized packages like Phojet and Cascade [17]. With these versatile tools at hand, we ware able to model and simulate a wide range of physics processes, enabling a comprehensive study of the collision events targeted in my analysis.

For the investigation of VBF HH, signal events were simulated at leading order (LO) using MadGraph5_aMC@NLO [18]. We used a customized model, allowing the generation of events for different combinations of κ_V, κ_{2V}, and κ_λ coupling values, providing a comprehensive exploration of the coupling parameter space (Figure 36 in Appendix). With this configuration, a total of 150,000 unweighted events were generated for each set of the arbitrarily chosen coupling values and for centre-of-mass energy of 13 TeV.

After generating parton-level events, the corresponding Les Houches event files for signal events are processed through the Pythia8 Monte Carlo generator within the ATLAS Athena framework. Within Pythia, specific commands are utilized to perform the showering process and simulate the decay channel of the two Higgs bosons, with a particular focus on the final state of $b\bar{b}\tau^-\tau^+$.(Figure 37 in Appendix.)

Given that our primary objective from the outset was to assess the influence of anomalous values on the VBF HH cross-section and to determine the proportion of boosted events with potential for future studies, a considerable number of samples needed to be generated. Relying solely on MadGraph for this purpose proved to be time-consuming (avg. 1-2 hours per simulation), as it required repeated iterations of the process involving VBF generation with various coupling parameter sets. To expedite the generation of diverse scenarios, we had to employ alternative methods for faster simulation of arbitrary coupling combinations.

4.1 Method for generating more VFB processes

As illustrated in Figure 4, the VBF HH production involves three main diagrams at LO. Consequently, we can express that the VBF cross-section is proportional to:

$$\sigma \sim |\mathscr{A}|^2 = |A + B + C|^2 \tag{4.1}$$

where "A" corresponds to the HHH diagram, "B" to the VVH diagram, and "C" to the VVHH diagram. Taking into consideration the coupling values and interferences between the various Feynman diagrams, we can now express Equation 4.1 as follows:

$$\sigma \sim \kappa_V^2\kappa_\lambda^2 A^2 + \kappa_V^4 B^2 + \kappa_{2V}^2 C^2 + \kappa_V^3\kappa_\lambda I_{AB} + \kappa_{2V}\kappa_V\kappa_\lambda I_{AC} + \kappa_V^2\kappa_{2V} I_{BC} \tag{4.2}$$

Where interferences are defined as:

$$I_{AB} = |A^*B + AB^*|\,, I_{AC} = |A^*C + AC^*|\,, I_{BC} = |B^*C + BC^*| \tag{4.3}$$

In Equation 4.2, we encounter six unknown values (A, B, C, I_{AB}, I_{AC}, I_{BC}). To address this, our approach involved generating six distinct VBF processes using MadGraph. This allowed us to establish a system of six equations corresponding to the six unknown parameters. We can describe this system in terms of matrices, using the following notation:

$$\vec{\sigma} = \begin{pmatrix} \sigma_1 \\ \sigma_2 \\ \sigma_3 \\ \sigma_4 \\ \sigma_5 \\ \sigma_6 \end{pmatrix}, \vec{\kappa} = \begin{pmatrix} \kappa_V^2\kappa_\lambda^2 \\ \kappa_V^4 \\ \kappa_{2V}^2 \\ \kappa_V^3\kappa_\lambda \\ \kappa_{2V}\kappa_V\kappa_\lambda \\ \kappa_V^2\kappa_{2V} \end{pmatrix}, \vec{c} = \begin{pmatrix} A \\ B \\ C \\ I_{AB} \\ I_{AC} \\ I_{BC} \end{pmatrix}, \tag{4.4}$$

where we defined cross-section, vector of coupling and vector of components. Last thing we

had to define is a matrix M that represents the following:

$$\mathbf{M} = \begin{bmatrix} \kappa_{V_1}^2\kappa_{\lambda_1}^2 & \kappa_{V_1}^4 & \kappa_{2V_1}^2 & \kappa_{V_1}^3\kappa_{\lambda_1} & \kappa_{2V_1}\kappa_{V_1}\kappa_{\lambda_1} & \kappa_{V_1}^2\kappa_{2V_1} \\ \kappa_{V_2}^2\kappa_{\lambda_2}^2 & \kappa_{V_2}^4 & \kappa_{2V_2}^2 & \kappa_{V_2}^3\kappa_{\lambda_2} & \kappa_{2V_2}\kappa_{V_2}\kappa_{\lambda_2} & \kappa_{V_2}^2\kappa_{2V_2} \\ \kappa_{V_3}^2\kappa_{\lambda_3}^2 & \kappa_{V_3}^4 & \kappa_{2V_3}^2 & \kappa_{V_3}^3\kappa_{\lambda_3} & \kappa_{2V_3}\kappa_{V_3}\kappa_{\lambda_3} & \kappa_{V_3}^2\kappa_{2V_3} \\ \vdots & \vdots & \vdots & \vdots & \vdots & \vdots \\ \vdots & \vdots & \vdots & \vdots & \vdots & \vdots \\ \kappa_{V_6}^2\kappa_{\lambda_6}^2 & \kappa_{V_6}^4 & \kappa_{2V_6}^2 & \kappa_{V_6}^3\kappa_{\lambda_6} & \kappa_{2V_6}\kappa_{V_6}\kappa_{\lambda_6} & \kappa_{V_6}^2\kappa_{2V_6} \end{bmatrix} \tag{4.5}$$

In equations 4.4 and 4.5, the matrices $\vec{\sigma}$ and $\mathbf{M}$ are populated with the values obtained from our simulations. With this notation, Equation 4.2 can be written as:

$$\vec{\sigma} = \mathbf{M} \cdot \vec{c}, \tag{4.6}$$

from which we can compute values for the vector of components:

$$\vec{c} = \mathbf{M}^{-1} \cdot \vec{\sigma}. \tag{4.7}$$

The primary purpose of employing this matrix method is to enable the computation of cross-sections for any combination of coupling values. This description equally holds for the total cross section as well as the differnetial cross section. The computation of cross-sections becomes possible once we have acquired the cross-sections for the six distinct configurations of coupling parameters and using :

$$\begin{aligned} \sigma &= \vec{\kappa}^{\intercal} \cdot \vec{c}, \\ \sigma &= \vec{\kappa}^{\intercal}\mathbf{M}^{-1}\vec{\sigma}. \end{aligned} \tag{4.8}$$

With equations 4.7 and 4.8 at our disposal, we possessed the necessary tools to advance in our investigation of VBF HH. This approach allowed us to significantly reduce the time spent waiting for individual simulations with varying couplings, as we could now swiftly compute their outcomes. The only thing we had to be careful about was selecting suitable coupling values to fill the matrix M with, ensuring its invertibility. Therefore, we generated six distinct sets of coupling values tailored for the proper functioning of this method. The coupling values and their corresponding cross-sections used in this method can be found in Table 2.

We can also compute the the distribution of amplitudes by using Eq. 4.7 as shown in Figure 15. From Figure 15, it is evident that a cancellation occurs between I_{AB} and I_{AC}, as well as between I_{BC} and B. This outcome was anticipated, aligning with the statement made in Equation 2.10 that these amplitudes are suppressed within the context of the Standard Model.

κ_V	κ_{2V}	κ_λ	σ [pb]
1	0	-3	0.05727
1	1	1	0.001226
1	2	1	0.009959
1	0	3	0.01067
1	0	4	0.00945
1.5	1	1	0.04531

Table 2: *Coupling values and corresponding cross-sections used for the explained method*

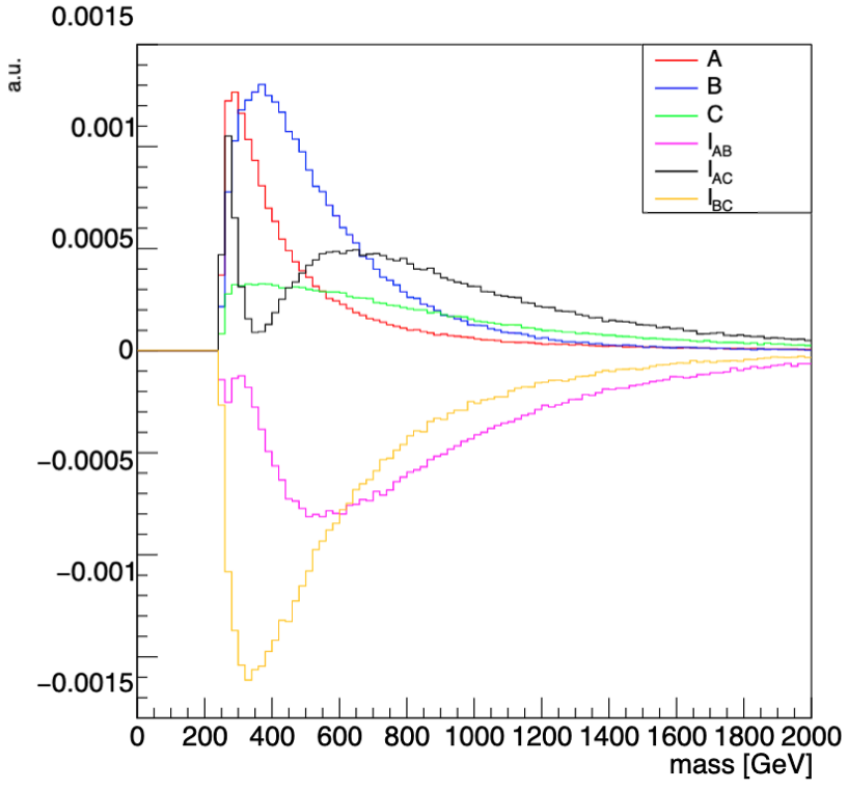

Figure 15: *Distributions of the amplitudes. Y-axis units are arbitrary, but the relative normalization of the various curves is proportional to the cross section associated with each amplitude.*

In addition to calculating the cross section using Equation 4.8, we can extend the same methodology to analyze various variables of interest. Let's take the example of studying the dependence of the variable m_{HH} for a specific set of couplings. To achieve this each of the six m_{HH} histograms obtained from our earlier simulations is scaled using its corresponding scaling factor derived from Equation 4.8. Since Equation 4.8 is composed of the sum of six parameters, we initiate by scaling the histogram from our simulations. For example, the one histogram corresponding to couplings in the first row of the inverse matrix M and with the cross section value from the first component of the sigma matrix, we scale utilizing the first parameter from the equation. Similarly, we apply this scaling procedure to each of the six m_{HH} histograms previously derived from our simulations, utilizing their corresponding scaling factors stemming from Equation 4.8. Following this step, we sum all these scaled histograms, resulting in the

final histogram that encapsulates crucial insights into the m_{HH} dependency on the selected couplings. Validation of this method, including m_{HH} and other key variables, is presented in Section 5.1.1.

5 Results

In the preceding section, we detailed the results of generating VBF production events of Higgs boson pairs using MadGraph5_aMC@NLO. Through this process, we had the capability to manipulate coupling parameters, thereby generating events that depart from the predictions of the SM. For each of the coupling values, we generated at least six different cases in which we varied the value of the particular coupling while keeping the other two at their SM values.

5.1 HH production results

Initially, our goal was to determine if anomalous values could lead to an increase in the VBF production rate. Therefore, it became imperative to study the cross-section's dependency on specific coupling values. For each coupling value, we deduced the relationship of the cross-section, and subsequently, we employed the chi-squared method to determine the best-fitting function, based on theoretical predictions, using the data generated from MadGraph.

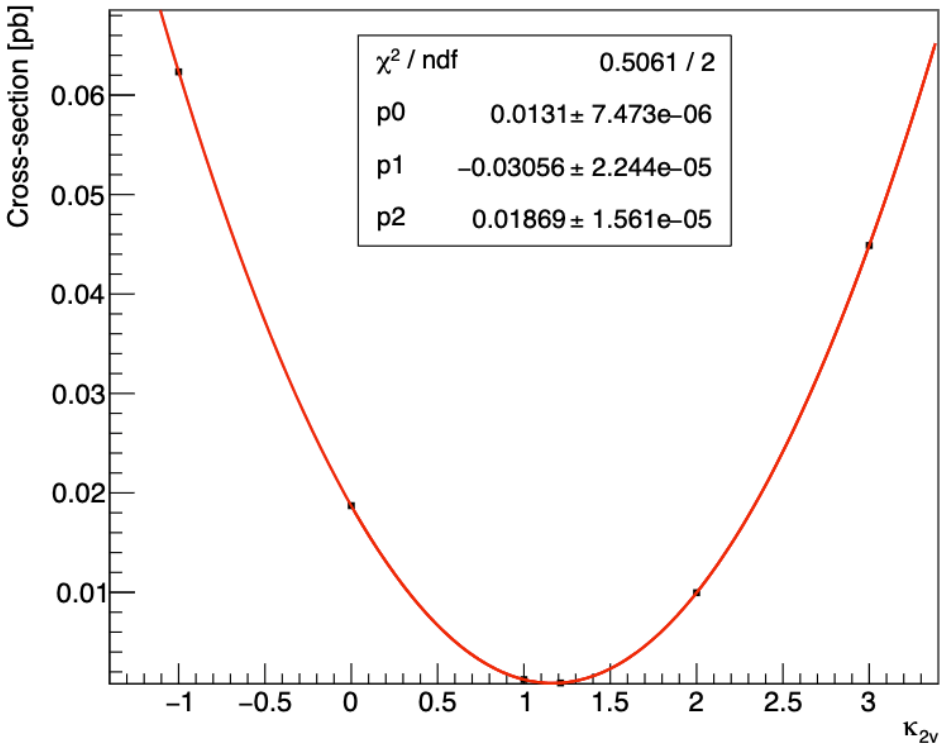

Figure 16: *Observed values (black dots) and chi-squared fit (red line) of the VBF HH production cross section as a function of the κ_{2V} coupling, with other couplings fixed to the SM values.*

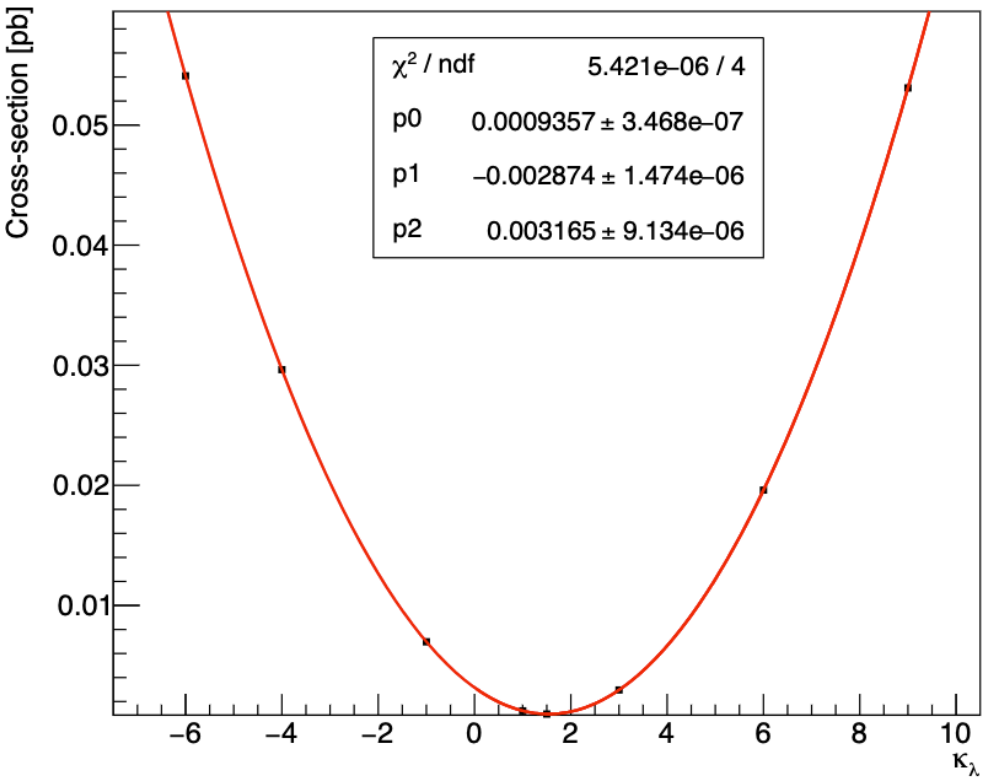

Figure 17: *Observed values (black dots) and chi-squared fit (red line) of the VBF HH production cross section as a function of the κ_λ coupling, with other couplings fixed to the SM values.*

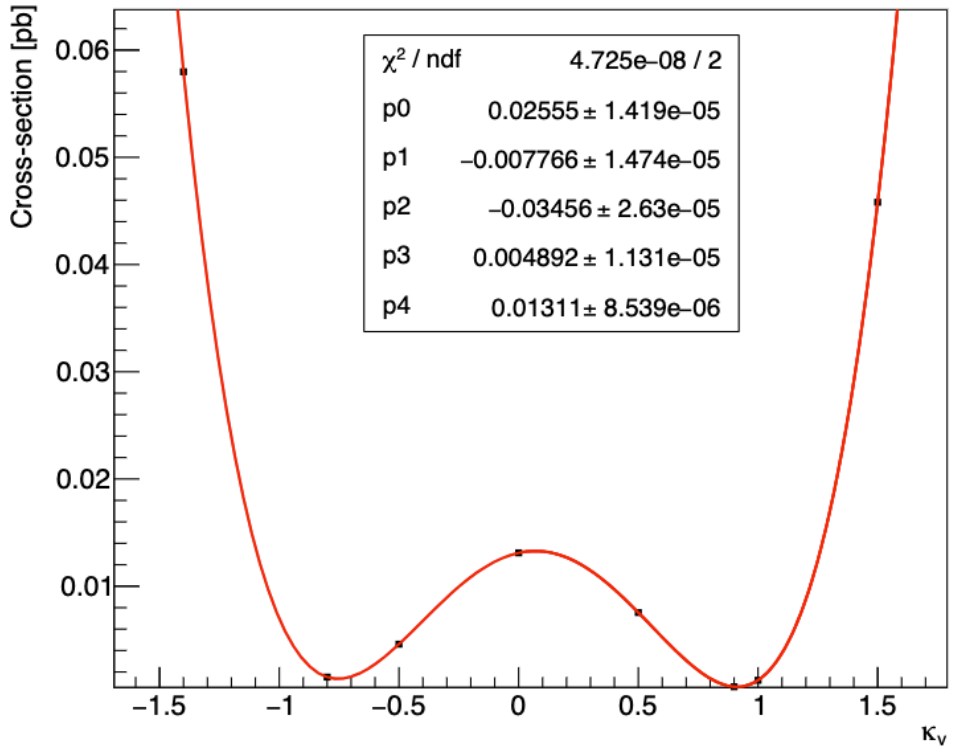

Figure 18: *Observed values (black dots) and chi-squared fit (red line) of the VBF HH production cross section as a function of the κ_V coupling, with other couplings fixed to the SM values.*

From Fig. 16, Fig. 17, and Fig. 18, it's evident that anomalous values of the couplings have a significant impact on the cross section. Specifically, variations in the coupling values amplify the VBF production rate. For κ_{2V} and κ_λ, the cross section shows a parabolic dependence, with the corresponding parameters and errors illustrated in the respective figures. In contrast, for κ_V, our generated values correspond to the theoretical dependence of a 4th-order polynomial function. A comparison of these three figures reveals that the production rate increases notably for anomalous values. The most significant impact is observed in Figure 16 for the κ_{2V} dependence, whereas for κ_λ, the effects are minor, requiring larger coupling variations for the same change in cross section.

Another important aspect we aim to investigate is the dependence on m_{HH} since we are interested in studying VBF HH in the high-mass range. Figures 19 and 20 illustrate that the m_{HH} distributions vary significantly for anomalous coupling values, showing an increase in the distribution at higher masses.

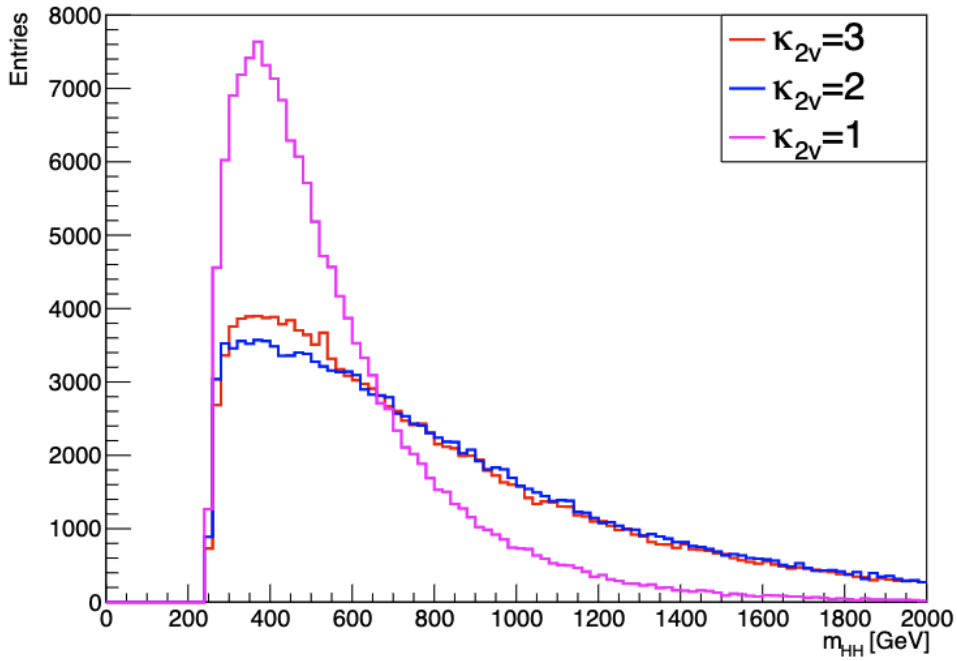

Figure 19: *Distribution of m_{HH} for VBF HH events for the SM (purple) and for anomalus values of κ_{2V}*

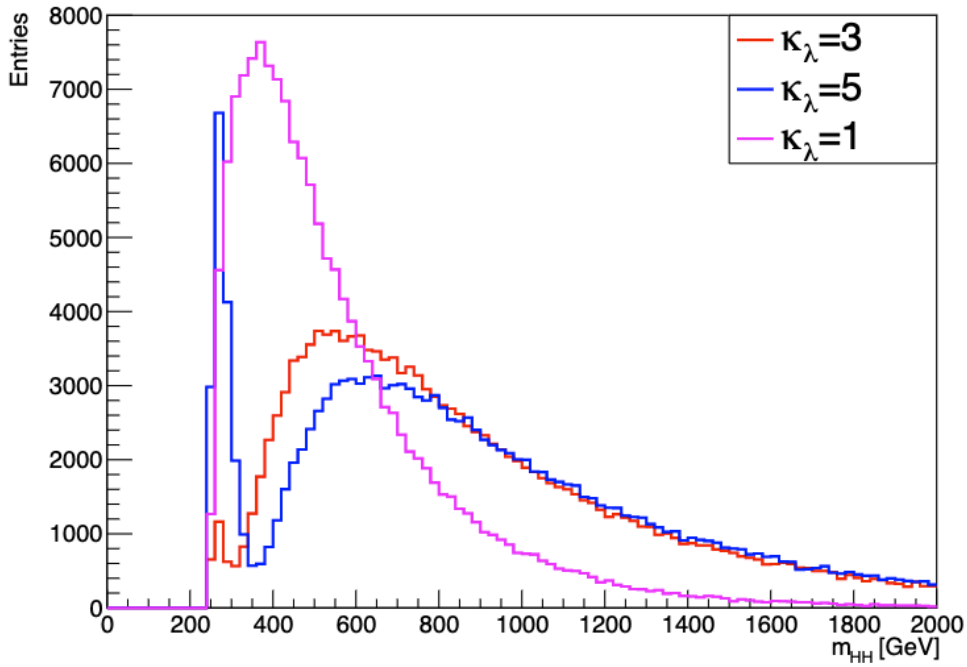

Figure 20: *Distribution of m_{HH} for VBF HH events for the SM (purple) and for anomalus values of κ_λ*

As mentioned in the Introduction, the VBF process is defined by the presence of two widely separated jets. In the context of our analysis, "jet 1" and "jet 2" represent the highest-energy jets arising from the vector boson fusion (VBF) mechanism. These jets play a pivotal role in the VBF process, acting as indicators of the initial quarks or gluons involved in the collision that ultimately give rise to the Higgs boson pairs. Jet 1 is characterized by having the higher energy of the two, while jet 2 possesses slightly less energy but is still considerably energetic. When we delve into plotting rapidities for these jets, we are essentially exploring the spatial orientation of their movement along the beamline. This investigation offers insights into the behavior of the particles involved in the collision and their momentum distributions. In the forthcoming figures, derived from our simulations with anomalous coupling values, we have successfully computed the pseudorapidity for various scenarios involving our outgoing jets.

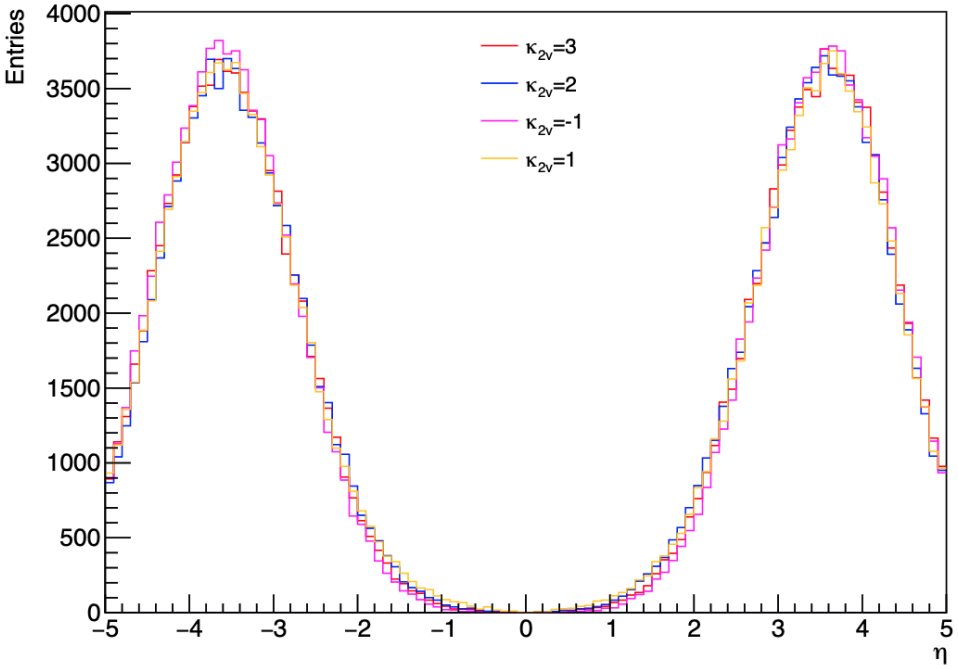

Figure 21: *Pseudorapidity of jet 1 from VBF HH process for different κ_{2V} values.*

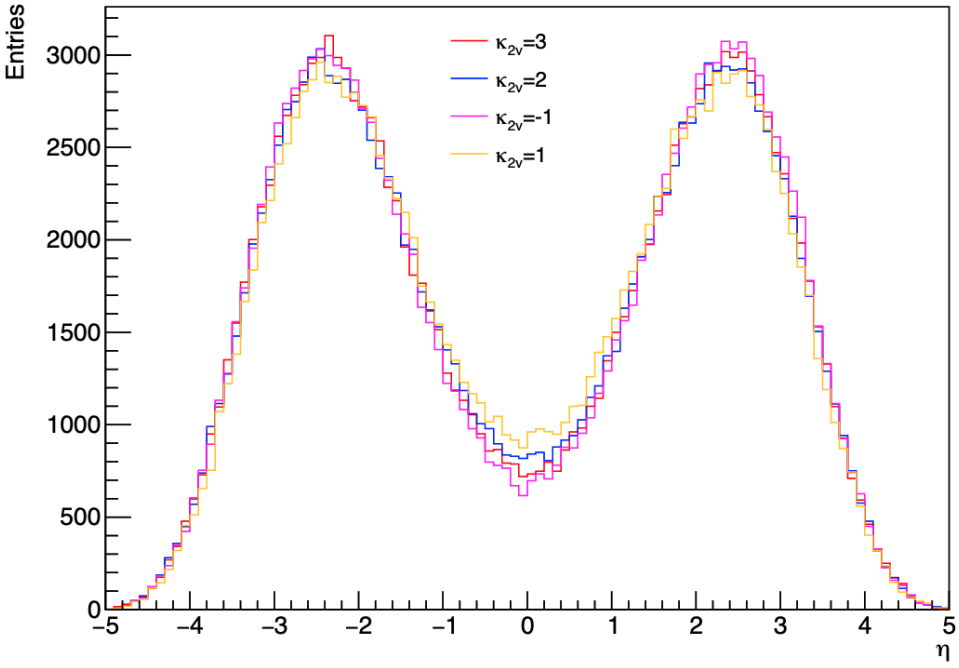

Figure 22: *Pseudorapidity of jet 2 from VBF HH process for different κ_{2V} values.*

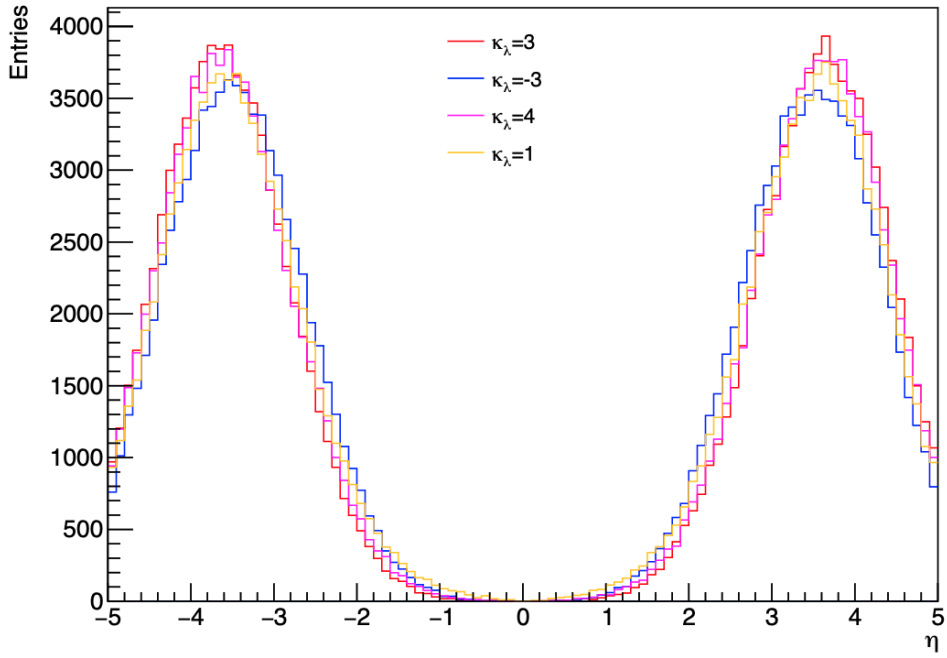

Figure 23: *Pseudorapidity of jet 1 from VBF HH process for different κ_λ values.*

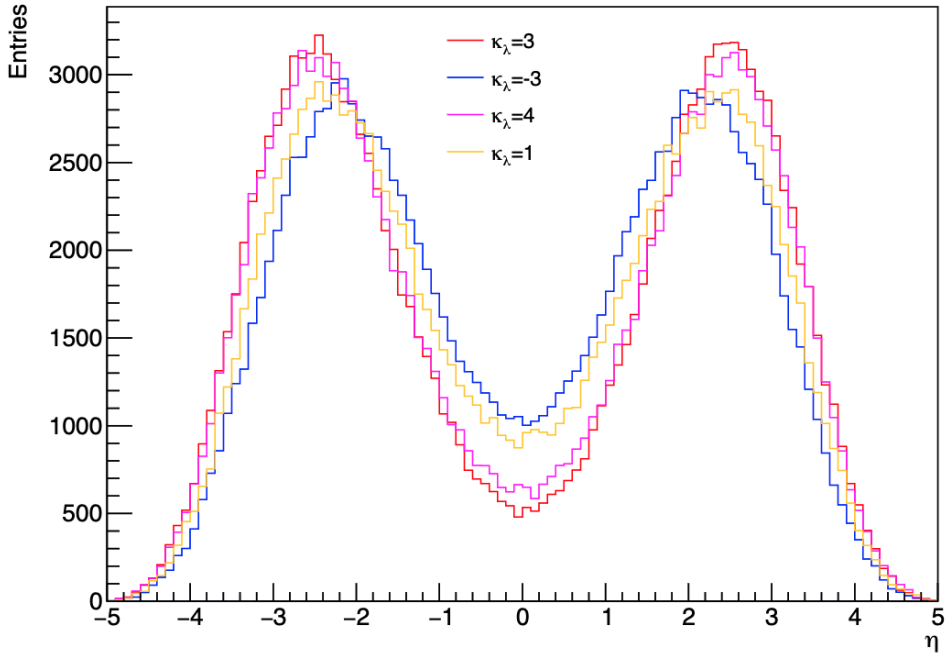

Figure 24: *Pseudorapidity of jet 2 from VBF HH process for different κ_λ values.*

Upon comparing Figure 21 with Figure 23, and Figure 22 with Figure 24, it is evident that the pseudorapidities of the jets from our simulations exhibit consistency, showing minimal deviation across different values of the coupling parameters. This consistency is significant as it provides valuable insights into the detectability of these jets. Notably, the majority of jet 1 pseudorapidities fall within the range of $3 < |\eta| < 4.5$, while jet 2 pseudorapidities predominantly lie within the range of $2 < |\eta| < 3.5$.

5.1.1 Validation of the Method 4.1

To validate the method described in Section 4.1, a comparison was necessary between the key distributions obtained in previous sections and those derived from this method. With all the necessary components in place, we are now capable of generating a substantial number of data points to comprehensively examine the influence of couplings on the VBF HH process. Our primary objective is to validate that the cross-section dependence derived from this method agrees with the dependencies we obtained from MadGraph.

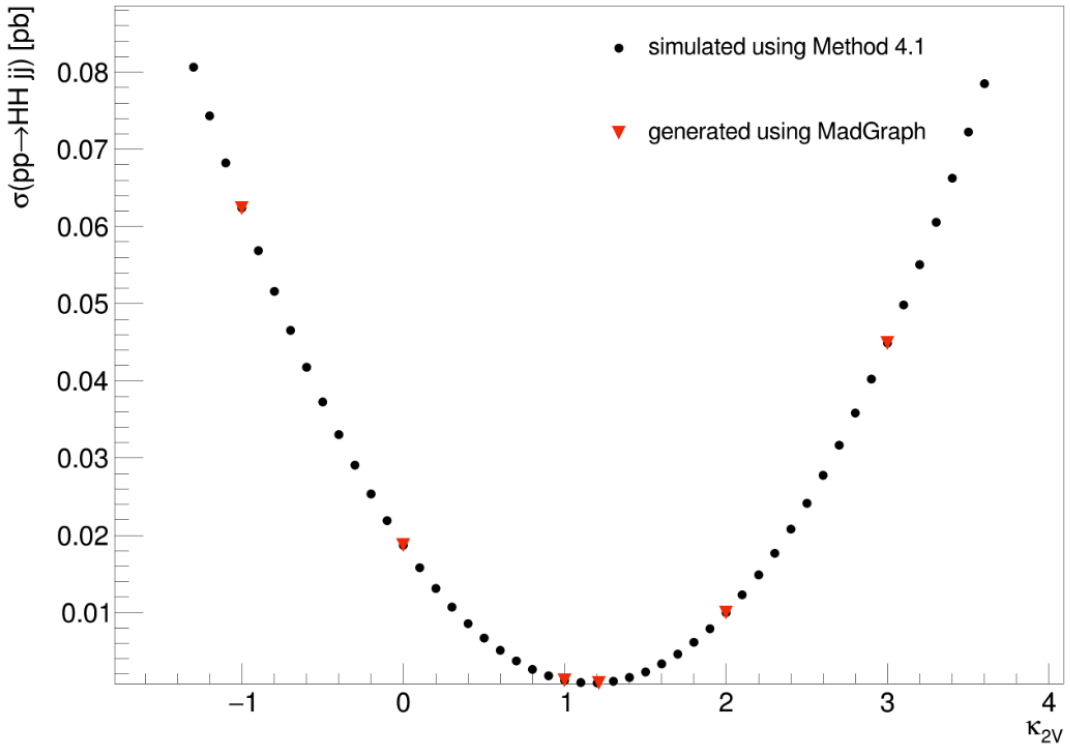

Figure 25: *Value of the VBF HH cross section as function of the coupling* κ_{2V}

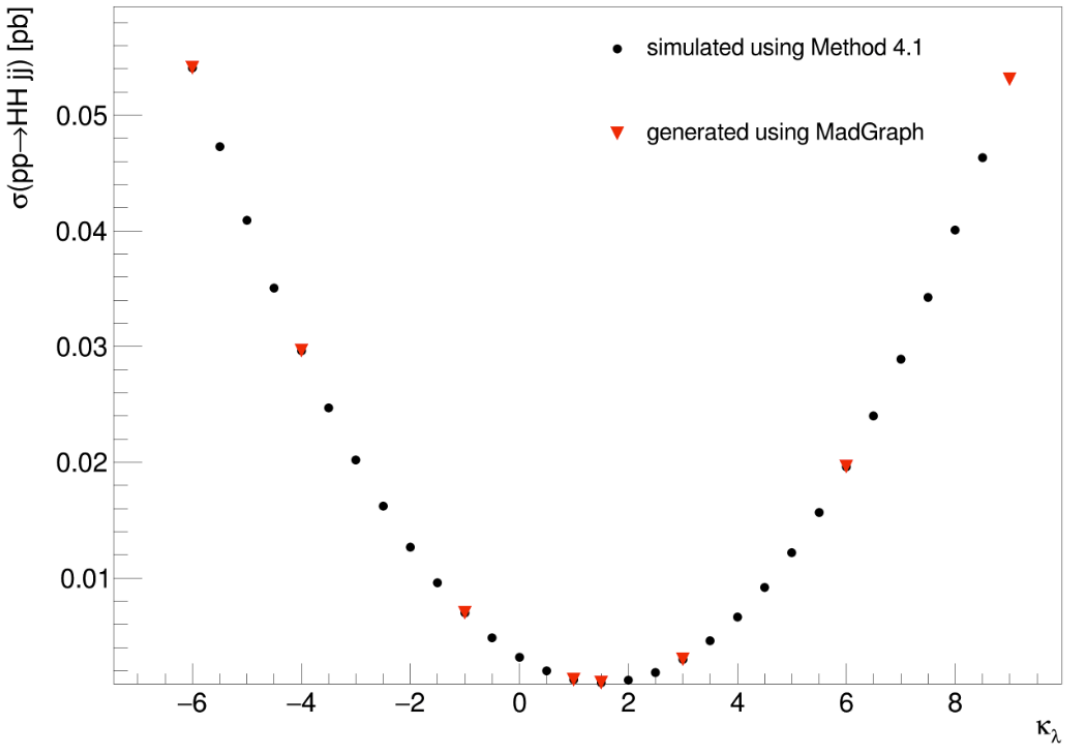

Figure 26: *Value of the VBF HH cross section as function of the coupling* κ_λ

Both Fig. 25 and Fig 26. demonstrate the consistency of our method and validate it when compared with the results from MadGraph.

In Section 4.1, we explain this method using the case of the m_{HH} distribution. Thus, we will also investigate whether our method is applicable to other distributions besides the cross-section. Following the steps we explained, we derived the m_{HH} distribution from the scaling of the six generated samples, and we also generated the distribution for the same set of coupling values from MadGraph. The distribution we obtained from MadGraph we also had to scale to properly compare the two distributions. Although we can see some fluctuations in both Fig. 27 and Fig. 28, the shape of our distributions is almost perfectly similar. This confirms the validation of this method once again.

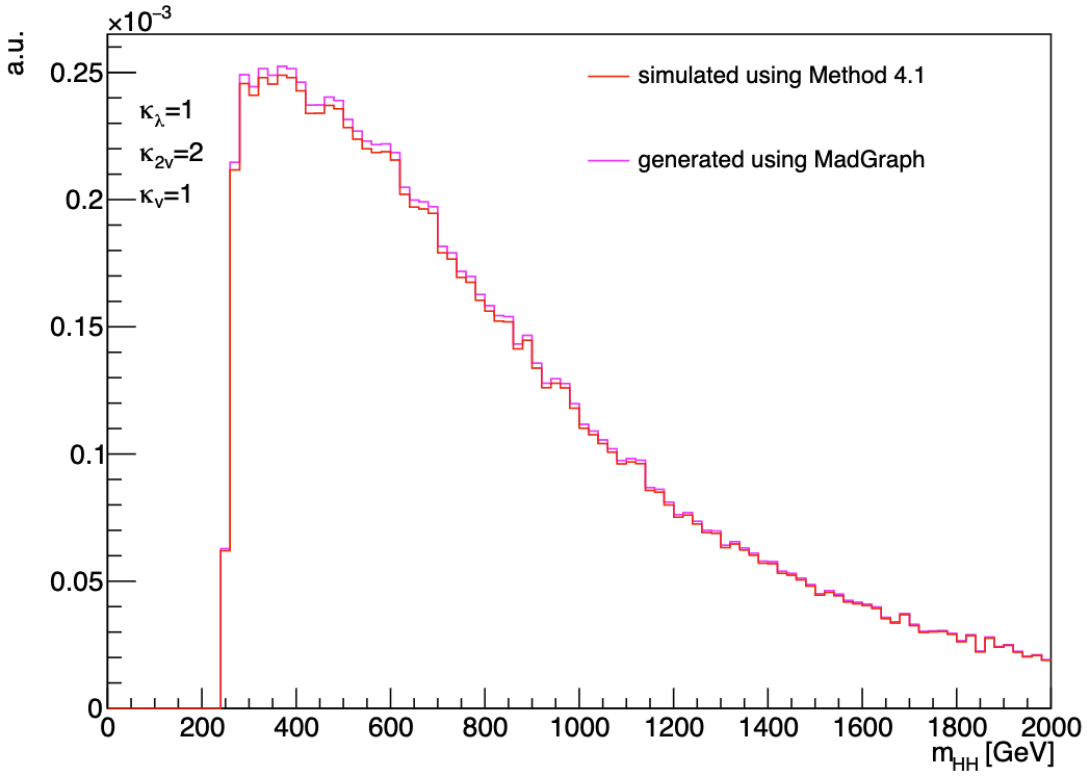

Figure 27: *Comparison of the m_{HH} distribution generated using MadGraph (purple) and simulated using our method (red).*

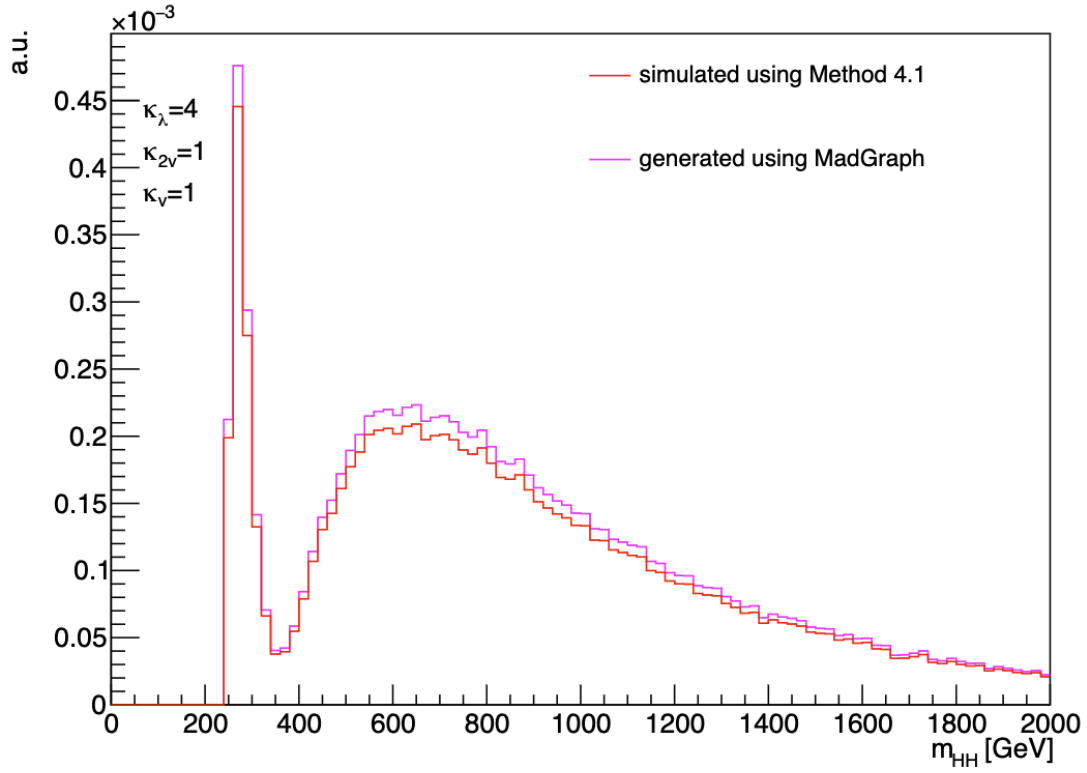

Figure 28: *Comparison of the m_{HH} distribution generated using MadGraph (purple) and simulated using our method (red).*

5.1.2 VBF HH boosted events

Finally, in this phase of our analysis, we are able to quantitatively assess the proportions of boosted events across various coupling scenarios. Our simulated events are categorized into three groups: boosted events, resolved events, and semi-resolved events. Boosted events involve both Higgs bosons having high transverse momentum (we used selection for $p_T > 300GeV$), semi-resolved events include at least one Higgs boson with high momentum, and resolved events have neither. Our focus is on understanding the prevalence of boosted events within these categories. From Figure 29, we observe that in the case of the Standard Model, there

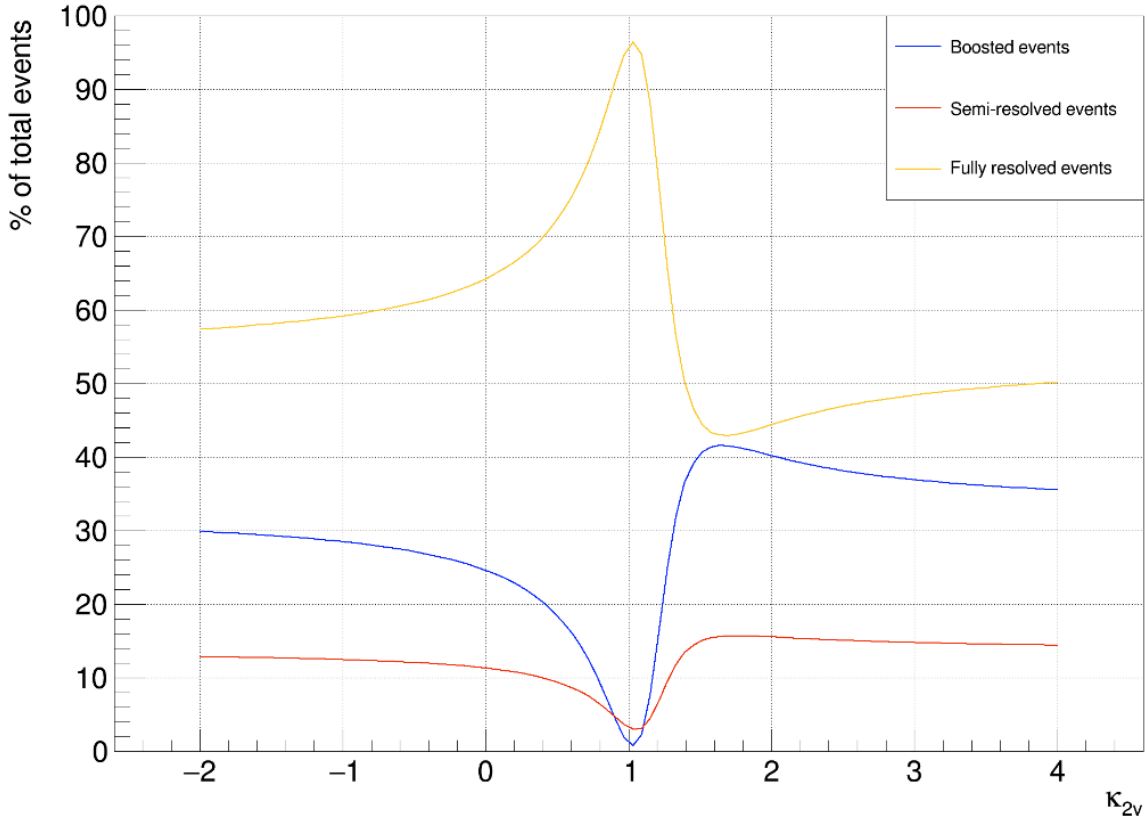

Figure 29: *Ratios of boosted, resolved and semi-resolved VBF events for anomalus κ_{2V} values.*

are relatively fewer of these "interesting" boosted events. However, as we move away from the Standard Model configuration, there is a notable increase in the occurrence of boosted events. Our simulation results reveal that the highest percentage of boosted events is associated with κ_{2V} values approximately around the [1.4,1.6] range. This aligns with our previous statement, where for anomalous values of coupling parameters we encountered enhancement in VFB production at high m_{HH}. Remarkably, these values fall just on the boundaries of the currently known constraints for κ_{2V}. For these specific κ_{2V} values, we observe slightly above 40% of the total events exhibiting the boosted characteristic. This finding implies that future analyses of VBF in the high p_T regime can be significantly enhanced.

5.2 $HH \rightarrow b\bar{b}\tau^+\tau^-$ results

Now, we proceed to the final phase of this analysis, focusing on the exploration of the decay channel involving τ leptons and b quarks. Since we want to study this decay in the boosted regime, and from the previous figure, we found that the highest percentage of boosted events occurs when κ_{2V} has a value of around 1.5, we mainly focused these coupling values in further study of the decay. As elaborated in section 4, we employed Pythia8 to execute the showering process and simulate the desired decay channel. Identifying and correctly associating the particles originating from the decay of τ leptons and b quarks are fundamental steps. The separation between the decay products of τ leptons and b quarks is important as we want to understand where they have low dR (dR<0.8), so decay particles can get reconstructed as a single large-radius jet. This separation is critical to constructing a coherent picture of the final state.

Additionally, in our analysis, we have implemented specific selection criteria to refine the data we study. These cuts are used to exclude events that either cannot be effectively detected by our particle detector or events that are not relevant to our study.

To achieve this, we have introduced constraints on the p_T of the particles. We have set a threshold that the transverse momentum must be greater than 20 GeV, which is a typical lower threshold for the triggering, reconstruction, and identification of b and τ jets. This criterion helps us focus on particles that carry a significant amount of momentum across the plane perpendicular to the beam direction.

Moreover, we have restricted the η of the particles. We require the pseudorapidity to be less than 2.5. This choice is motivated by our expectation that the decay products should fall within this pseudorapidity range. Our tracker in the ATLAS detector covers that range, which makes it possible to reconstruct and identify the decay particles.

By applying these cuts, we identify a subset of events where we expect high reconstruction and identification efficiencies, that can be used in the analysis.

In the context of τ decay channels, the situation can become intricate due to the multiple tau decays channels. Nevertheless, the particles emerging from the tau decays, can be identified and analyzed. Consequently, based on the distinct decay products arising from our taus, we have categorized them into three categories: fully-hadronic, fully-leptonic, and semi-leptonic di-τ final states. This classification depends on whether both taus yield hadronic particles, leptons, or a combination of both. The branching ratios of tau decays can be found in the Table 1.

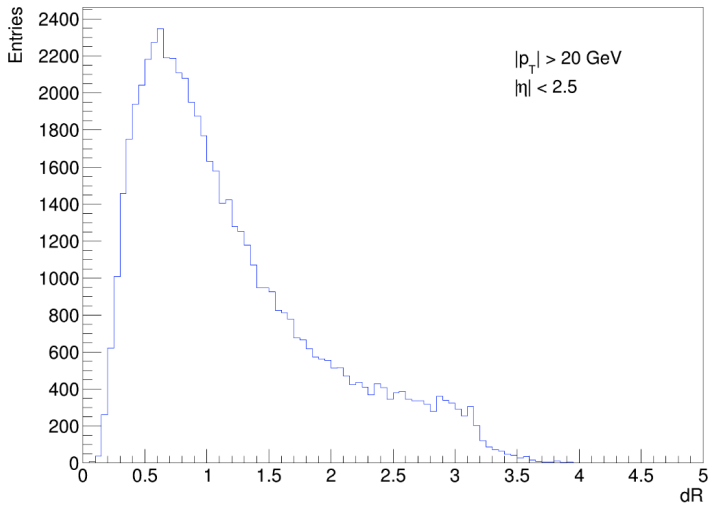

Figure 30: *Separation (dR) between two bottom quarks from $H \to b\bar{b}$ decay*

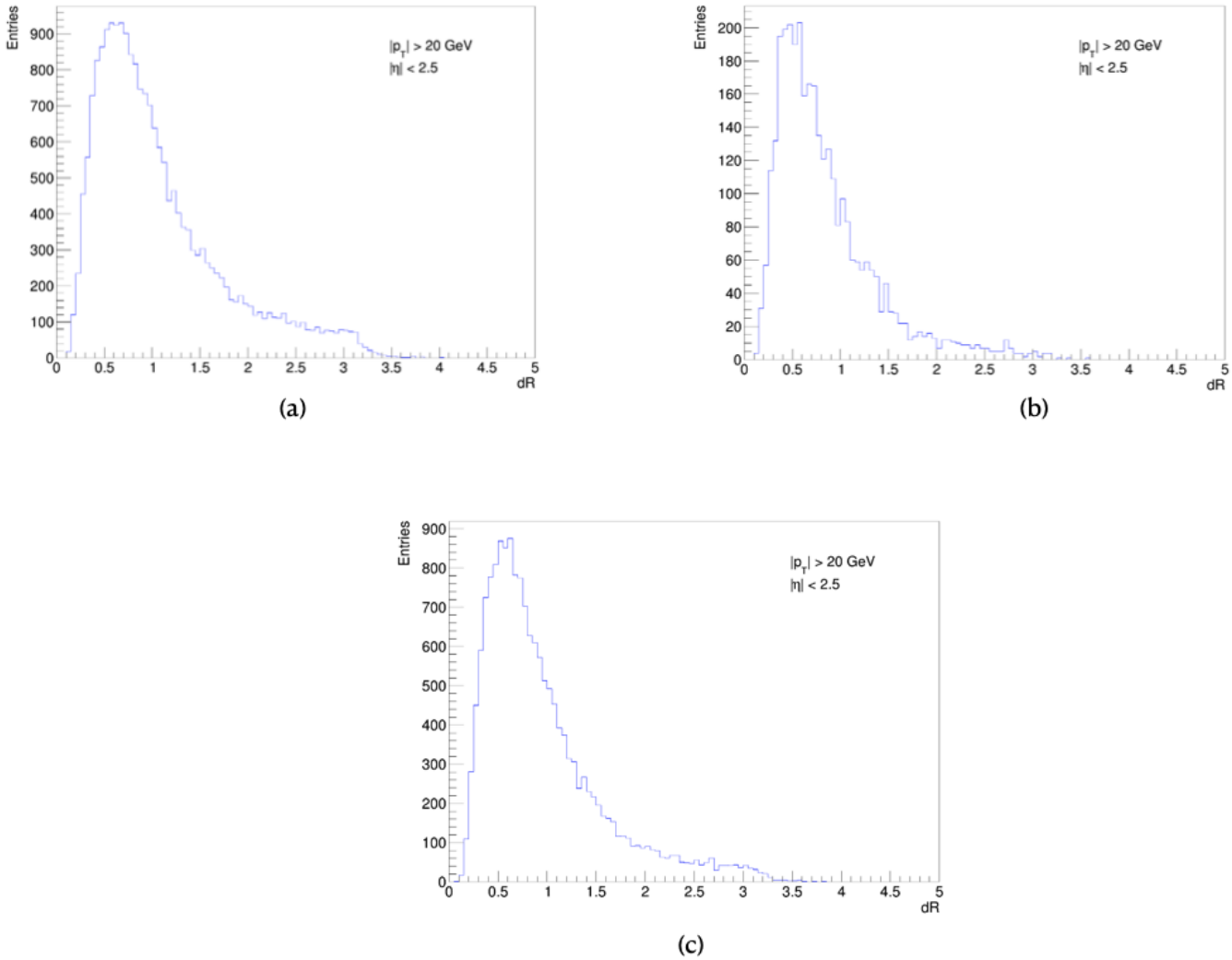

Figure 31: *Separation (dR) between two taus for $H \to \tau_{had}\tau_{had}$ (a), for $H \to \tau_{lep}\tau_{lep}$ (b) and for $H \to \tau_{lep}\tau_{had}$ (c).*

From the figures above, we can observe that the majority of events have a dR of around 0.8, which is advantageous as this constraint allows for the reconstruction of decay particles as a single large-radius jet.

In addition to the particle separation shown in Figures 30 and 31, Figure 32 presents the distributions of leading and sub-leading transverse momenta for both the b quarks and taus obtained from our simulations. This figure provides a closer examination of the transverse momentum characteristics of these particles, shedding light on their motion within the detector and their relevance in the decay process. In the context of our analysis, the terms "leading" and "subleading" refer to the transverse momenta of b quarks and taus. The "leading" particle, whether it's a b quark or a tau, corresponds to the one with the higher transverse momentum, signifying its greater energy in the direction perpendicular to the beam axis. Conversely, the "subleading" particle possesses a slightly lower transverse momentum, yet it remains of considerable significance in terms of energy. By plotting the transverse momenta of these particles, we gain insights into their energy distributions orthogonal to the beam axis. This exploration not only sheds light on the energetic behavior of the particles themselves but also provides valuable information about their interactions during the collision process.

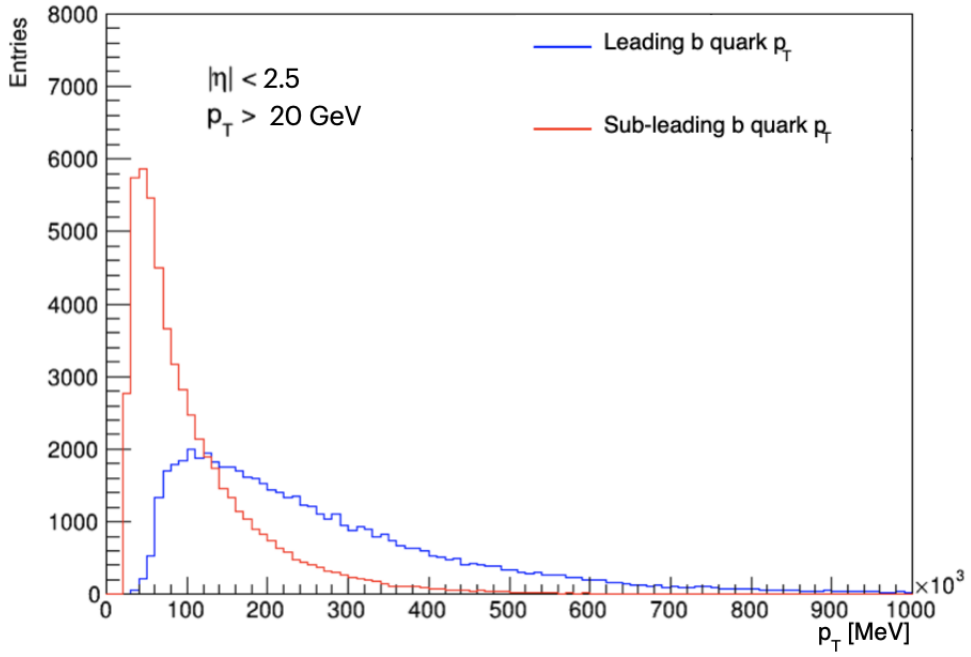

(a)

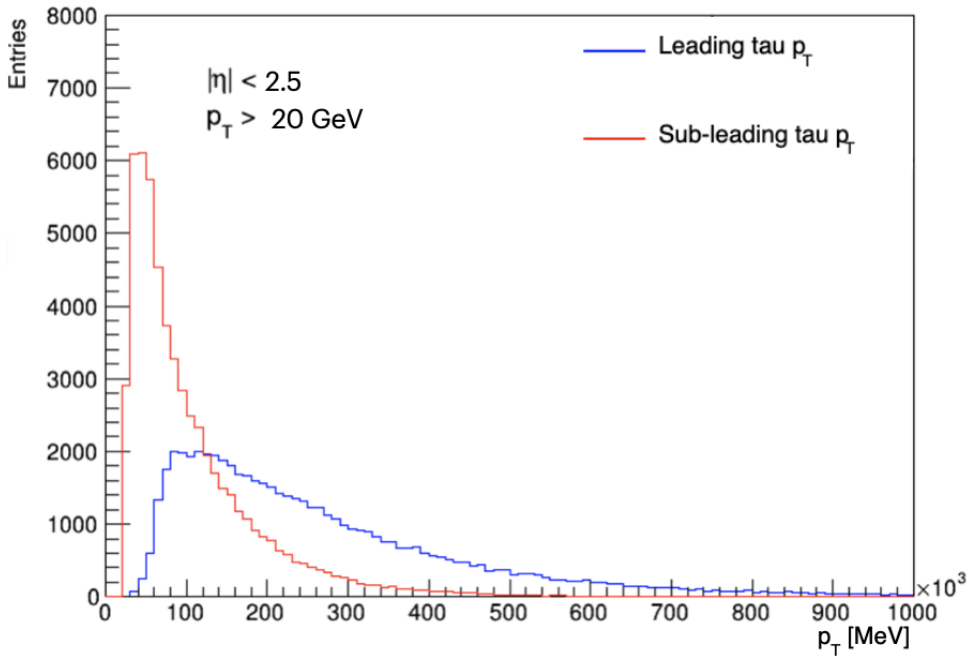

(b)

Figure 32: *Leading and sub-leading transverse momentum's for b quarks (a), and for taus (b)*

Utilizing Pythia8 for simulating the decay channel of di-Higgs, especially in the context of $H \rightarrow \tau\tau$, enables us to compare the tau before and after decay to see the impact of undetected momentum from neutrinos. As we highlighted earlier and visualized in previous graphs, the study of taus often involves analyzing their decay products due to their limited lifetime. However, Pythia enables us to generate plots for both τ_{vis} (representing detected decay products) and τ_{truth} (initial taus before decay). By plotting the mass distributions for these two

variables, as shown in Figure 33, τ_{truth} distribution exhibits a peak around 1777 MeV, matching the exact mass of the tau lepton. On the other hand, the τ_{vis} distribution displays several peaks, each corresponding to specific particles resulting from the tau decay process, such as electrons, muons, pions, kaons as well as ρ and a mesons. This was expected as we earlier in Section 2.4 described the leptonic and hadronic decay modes of τ.

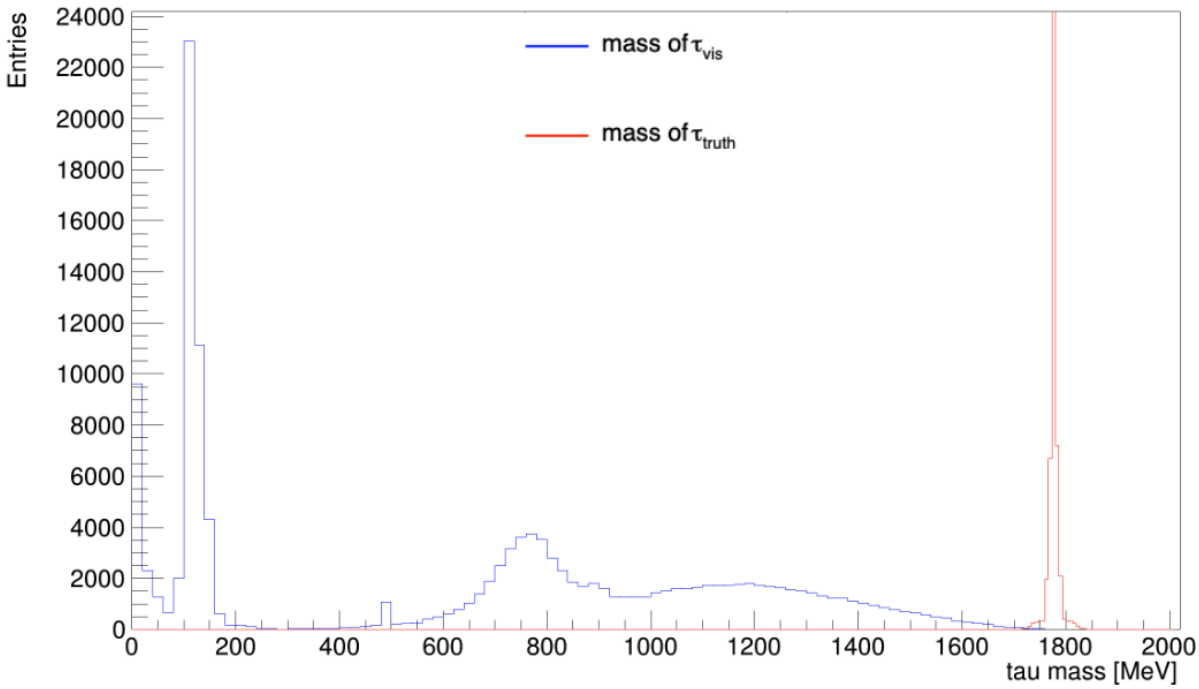

Figure 33: *Mass distribution of tau_visible (blue) and tau_truth (red)*

With this analysis, we can study the impact of neutrinos in the decay. The outcome of the comparison of transverse momenta of τ_{vis} and τ_{truth} is illustrated in Figure 34. Notably, Figure 34 reveals a consistent trend: the transverse momentum of visible taus consistently falls below that of the truth taus. This phenomenon can be attributed to the involvement of neutrinos in tau decays. The presence of neutrinos introduces a component of undetected energy, leading to what is commonly known as "missing energy." Despite neutrinos being elusive to direct detection, the comparison of transverse momenta allows us to indirectly gauge the influence of this missing energy on the observable decay products.

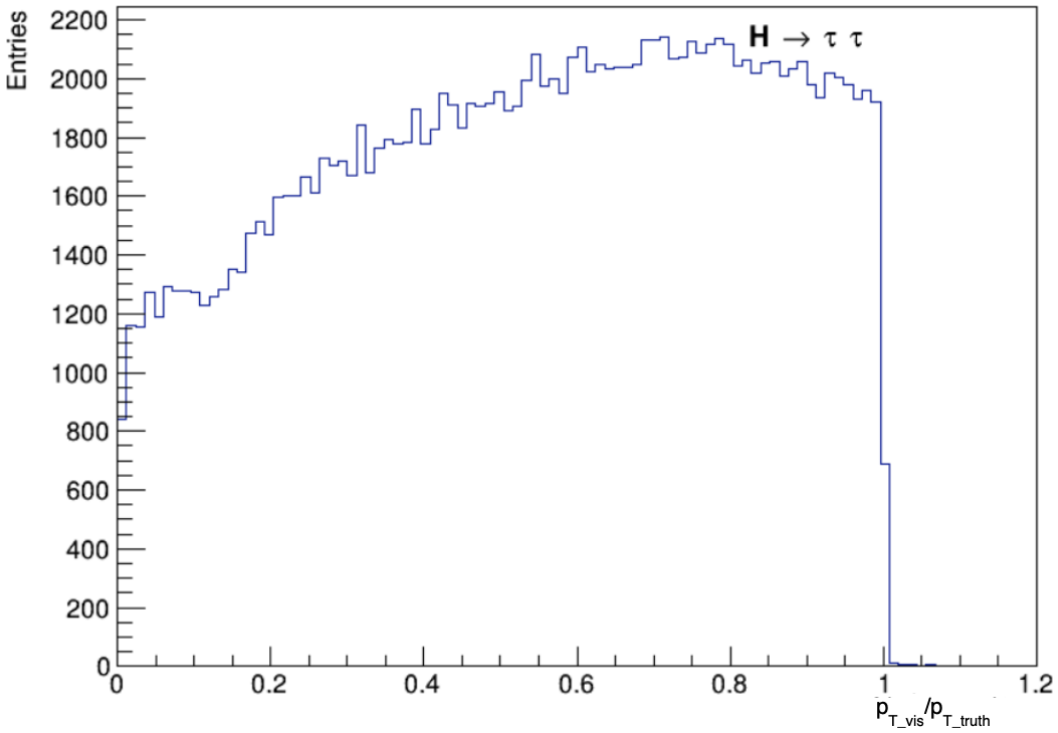

Figure 34: *Ratio of transverse momentum of τ_{vis} and τ_{truth}*

Just like in our previous section, which concentrated on the VBF production of di-Higgs, our current objective remains centered on segregating events primarily according to their boosted topology. The ultimate aim is to thoroughly analyze data from both run 2 and run 3 for this specific decay process. For the boosted events, our priority is to understand how anomalous values correlate with the event types. Drawing an analogy from our prior approach, we distinguished events into boosted, resolved, and semi-resolved categories, once again.

Additionally, we have applied the same constraints on the transverse momentum and pseudorapidity of b quarks and taus, as we did in previous distributions. The separation into three categories is depicted in Figure 35. We can observe that, once again, for values of κ_{2V} just under 2, the fraction of boosted events is at its maximum. Figure 35 also shows that for these coupling values, we can reach up to 60% of the total events that exhibit the boosted characteristic, if we were to include both fully boosted and semi-boosted events.

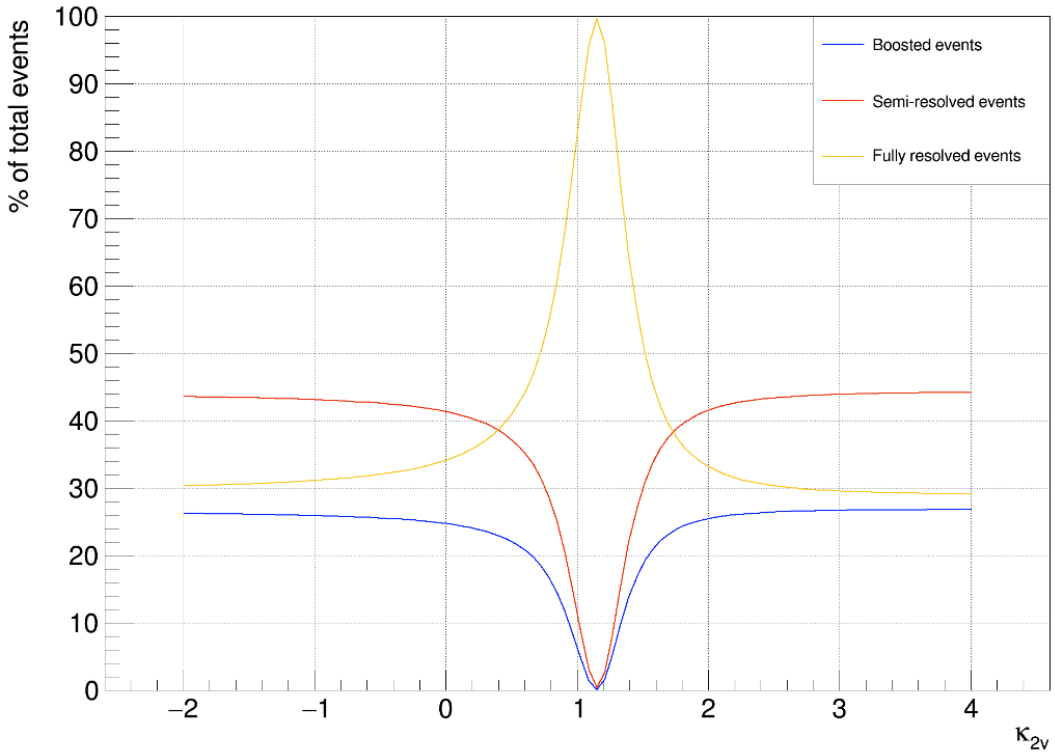

Figure 35: *Ratios of boosted, resolved and semi-resolved decay events for anomalus κ_{2V} values.*

6 Conclusion

The study presented in this thesis on the VBF production mode of Higgs boson pairs offers a valuable foundation for forthcoming ATLAS analyses, that will utilize data collected from both past and future LHC runs. In the initial phase of our analysis, we have delved into the impact of anomalous values for couplings, representing the interaction strength between Higgs bosons themselves or with vector bosons, on the production rate of Higgs boson pairs via vector boson fusion. Our exploration has revealed that anomalous values of κ_V or κ_{2V} can significantly enhance the VBF HH production rate at higher m_{HH} values. Moreover, our investigation has extended to the realm of boosted topology in the VBF context. Notably, we found that, for specific coupling values, our current analysis could be amplified by up atleast 40 percent. This encouraging outcome propels us to further explore VBF in this specific region.

In the second phase, we explored the $HH \rightarrow b\bar{b}\tau\tau$ decay channel, shedding light on the characteristics of the decayed particles, encompassing both b quarks and taus. In our analysis of taus resulting from Higgs decay, we segmented the properties into three distinct cases based on the decay products of the tau itself. The utilization of ATLAS software tools enabled us to calculate the properties of these particles, particularly emphasizing the consideration of missing momentum due to potential neutrinos from tau decay. All of this comprehensive information stands to amplify our future explorations, furnishing a great foundation for comparing data with simulations. Once again, we applied the boosted topology to this decay channel, in alignment

with our focus on searches within the boosted regime, and concluded that we can significantly enhance our analysis by including both boosted and semi-boosted events in the forthcoming investigations.

7 Bibliography

[1] The ATLAS Collaboration, *Observation of a New Particle in the Search for the Standard Model Higgs Boson with the ATLAS Detector at the LHC*, arXiv:1207.7214 [hep-ex] URL: https://doi.org/10.48550/arXiv.1207.7214

[2] The CMS Collaboration, *Observation of a new boson at a mass of 125 GeV with the CMS experiment at the LHC*, arXiv:1207.7235v2 [hep-ex] URL: https://doi.org/10.48550/arXiv.1207.7235

[3] The ATLAS Collaboration, *Combination of searches for non-resonant and resonant Higgs boson pair production in the* $\mathrm{bb}\gamma\gamma$*,* $\mathrm{bb}\tau^+\tau^-$*, and* bbbb *decay channels using* pp *collisions at* $\sqrt{s} = 13\ \mathrm{TeV}$ *with the ATLAS detector*, ATLAS-CONF-2021-052, URL: https://cds.cern.ch/record/2786865/files/ATLAS-CONF-2021-052.pdf

[4] Brost E. and Cadamuro L., *Searching for Pairs of Higgs Bosons in the LHC Run 2 Dataset*, Symmetry. 2022; 14(7):1467. URL: https://doi.org/10.3390/sym14071467

[5] Mark Thomson, *Modern Particle Physics*, Cambridge University Press, 2013

[6] Wikipedia, Standard Model, URL: https://en.wikipedia.org/wiki/Standard_Model(17. 7. 2023.)

[7] The ATLAS Collaboration, *Observation of a New Particle in the Search for the Standard Model Higgs Boson with the ATLAS Detector at the LHC*, arXiv:1207.7214 [hep-ex] URL: https://doi.org/10.48550/arXiv.1207.7214

[8] Arbey A. and Mahmoudi F., *Dark matter and the early Universe: a review*, arXiv:2104.11488v1 [hep-ph] URL: https://arxiv.org/pdf/2104.11488.pdf

[9] Degrassi G., Di Vita S., Elias-Miró J., R. Espinosa J., F. Giudice G., Isidori G., Strumia A., *Higgs mass and vacuum stability in the Standard Model at NNLO*, arXiv:1205.6497v2 [hep-ph] URL: https://arxiv.org/abs/1205.6497

[10] Baglio J., Djouadi A., Grober R., Muhlleitner M.M., Quevillon J., Spira M., *The measurement of the Higgs self-coupling at the LHC: theoretical status*, arXiv:1212.5581v2 [hep-ph], URL: https://doi.org/10.48550/arXiv.1212.5581

[11] The CMS Collaboration, *Search for nonresonant pair production of highly energetic Higgs bosons decaying to bottom quarks*,arXiv:2205.06667v2 [hep-ex] URL: https://arxiv.org/pdf/2205.06667.pdf

[12] The CMS Collaboration, *Search for Higgs boson pair production via vector boson fusion with highly Lorentz-boosted Higgs bosons in the four b quark final state at* $\sqrt{s}$ *= 13 TeV* URL: https://cds.cern.ch/record/2776802/files/B2G-21-001-pas.pdf

[13] ATLAS Open Data,
URL:http://opendata.atlas.cern/books/current/openatlasdatatools/_book/glossary.html
(17. 7. 2023.).

[14] The ATLAS Collaboration, *Transverse momentum, rapidity, and centrality dependence of inclusive charged-particle production in* $\sqrt{s_{NN}}$ *=5.02 TeV p+Pb collisions measured by the ATLAS experiment*, arXiv:1605.06436v2 [hep-ex]
URL:https://doi.org/10.48550/arXiv.1605.06436

[15] ResearchGate, URL: https://www.researchgate.net/figure/
The-overall-layout-of-the-ATLAS-Detector-The-z-axis-is-defined-by-the-beam-direction_
fig4_41217633 (20.7.2023.)

[16] The ATLAS Collaboration, *The ATLAS Experiment at the CERN Large Hadron Collider*, The ATLAS Collaboration et al 2008 JINST 3 S08003

[17] Journal of Physics: Conference Series, *Monte Carlo generators in ATLAS software*, C Ay et al 2010 J. Phys.: Conf. Ser. 219 032001,
URL:https://iopscience.iop.org/article/10.1088/1742-6596/219/3/032001/pdf

[18] Journal of Physics: Conference Series, *The automated computation of tree-level and next-to-leading order differential cross sections, and their matching to parton shower simulations*, arXiv:1405.0301v2 [hep-ph],
URL:https://doi.org/10.48550/arXiv.1405.0301

[19] Bishara F., Contino R., Rojo J., *Higgs pair production in vector-boson fusion at the LHC and beyond.*, Eur. Phys. J. C 77, 481 (2017),
URL:https://doi.org/10.1140/epjc/s10052-017-5037-9

[20] The CMS Collaboration, *Performance of reconstruction and identification of* τ *leptons decaying to hadrons and* ν *in* pp *collisions at* $\sqrt{s} = 13$ *TeV*, arXiv:1809.02816v3 [hep-ex], URL:https://arxiv.org/pdf/1809.02816.pdf

8 Appendix

```
# Setting parameters for param_card.dat
#------------------------------------------------------------------
parameters['NEW'] = {'CV':  '1.0000000',  # kappa_V
                     'C2V': '1.0000000',  # kappa_2V
                     'C3':  '1.0000000'}  # kappa_lambda

#------------------------------------------------------------------

parameters['MASS']={'25':'1.250000e+02'} #MH

#------------------------------------------------------------------
# Setting some parameters for run_card.dat
#------------------------------------------------------------------
extras = { 'lhe_version':'2.0',
           'cut_decays':'F',
           'scale':'125',
           'dsqrt_q2fact1':'125',
           'dsqrt_q2fact2':'125',
           'nevents':int(nevents)}

#------------------------------------------------------------------
# Generating non-resonant VBF-Only HH process with MadGraph
# Parameters are set above
#------------------------------------------------------------------
process="""
import model sm
define p = g u c d s u~ c~ d~ s~
define j = g u c d s u~ c~ d~ s~
import model /cvmfs/atlas.cern.ch/repo/sw/Generators/madgraph/models/latest/HHVBF_UFO
generate p p > h h j j $$ z w+ w- / a j QED=4
output -f"""

process_dir = new_process(process)

#------------------------------------------------------------------
```

Figure 36: *MadGraph commands for generating non-resonant VBF HH process.*

```
# Pythia8 showering setup
#--------------------------------------------------------------
# initialize Pythia8 generator configuration for showering

from GeneratorFilters.GeneratorFiltersConf import ParentChildFilter
runArgs.inputGeneratorFile = runArgs.inputGeneratorFile

include("Pythia8_i/Pythia8_A14_NNPDF23LO_EvtGen_Common.py")

#--------------------------------------------------------------
# Edit merged LHE file to remove problematic lines
#--------------------------------------------------------------
include("Pythia8_i/Pythia8_Powheg.py")

#--------------------------------------------------------------------------------------------
# EVGEN Configuration
#--------------------------------------------------------------------------------------------
evgenConfig.generators = ["Powheg", "Pythia8"]
evgenConfig.description = "SM diHiggs production, decay to bbyy."

# Pythia8 showering
#--------------------------------------------------------------
include("Pythia8_i/Pythia8_Powheg_Main31.py")

genSeq.Pythia8.Commands += ['25:m0 = 125.0',
                            '25:onMode = off',
                            '25:onIfMatch = 5 -5',
                            '25:onIfMatch = 15 -15',
                            'ResonanceDecayFilter:filter = on',
                            'ResonanceDecayFilter:exclusive = on',
                            'ResonanceDecayFilter:mothers = 25',
                            'ResonanceDecayFilter:daughters = 5,5,15,15',
                            ]

#--------------------------------------------------------------
# Dipole option Pythia8
#--------------------------------------------------------------
genSeq.Pythia8.Commands += ["SpaceShower:dipoleRecoil = on"]

#--------------------------------------------------------------------------------------------
# Generator Filters
#--------------------------------------------------------------------------------------------
from GeneratorFilters.GeneratorFiltersConf import ParentChildFilter
filtSeq += ParentChildFilter("hbbFilter", PDGParent=[25], PDGChild=[5])
filtSeq += ParentChildFilter("HtautauFilter", PDGParent=[25], PDGChild=[15])
filtSeq.Expression = "hbbFilter and HtautauFilter"
```

Figure 37: *Pythia8 showering setup.*